Effect of processing parameters and thermal history on microstructure evolution and functional properties in laser powder bed fusion of 316L

Kaustubh Deshmukh ^a, Alex Riensche ^b, Ben Bevans ^b, Ryan J. Lane ^c, Kyle Snyder ^d, Harold (Scott) Halliday ^e, Christopher B. Williams ^a, Reza Mirzaeifar ^a, Prahalada Rao ^{b,a}

^a Department of Mechanical Engineering, Virginia Tech, Blacksburg, VA 24061, USA
 ^b Grado Department of Industrial and Systems Engineering, Virginia Tech, Blacksburg, VA 24061, USA
 ^c Department of Biomedical Engineering and Mechanics, Virginia Tech, Blacksburg, VA 24061, USA
 ^d Commonwealth Center for Advanced Manufacturing, Prince George County, VA 23842, USA
 ^e Center for Advanced Manufacturing, Navajo Technical University, Crownpoint, NM 87313, USA

Abstract

In this paper, we explain and quantify the causal effect of processing parameters and part-scale thermal history on the evolution of microstructure and mechanical properties in the laser powder bed fusion additive manufacturing of Stainless Steel 316L components. While previous works have correlated the processing parameters to flaw formation, microstructures evolved, and properties, a missing link is the understanding of the effect of thermal history. Accordingly, tensile test coupons were manufactured under varying processing conditions. Their microstructure-related attributes, e.g., grain morphology, size and texture; porosity; and microhardness were characterized. Additionally, the yield and tensile strengths of the samples were measured using digital image correlation. An experimentally validated computational model was used to predict the thermal history of each sample. The temperature gradients and sub-surface cooling rates ascertained from the model predictions were correlated with the experimentally characterized microstructure and mechanical properties. By elucidating the fundamental process-thermal-structure-property relationship, this work establishes the foundation for future physics-based prediction of microstructure and functional properties in laser powder bed fusion.

Keywords: Laser powder bed fusion, Stainless Steel 316L, microstructure evolution, characterization and tensile testing, thermal history simulation

Introduction

Objective and Motivation

The objective of this work is to explain and quantify the causal effect of processing 1.

1.1 parameters and part-level thermal history on the evolution of microstructures and mechanical properties in the laser powder bed fusion (PBF-LB/M) additive manufacturing (AM) of stainless steel 316L components. For tractability, herein we refer to the process by the popular acronym – LPBF. A fundamental insight into *the process-thermal-structure-property* relationship is critical for manufacturing LPBF parts with consistent and repeatable functional integrity [1].

In LPBF, as shown in Figure 1, metal powder is raked or rolled onto a build plate and melted layer-by-layer with a laser [2]. The LPBF process enables the fabrication of complex geometries that are often impossible with subtractive and formative manufacturing processes [3]. The process has gained significant interest in strategic industries such as aerospace, automotive, biomedical, and energy generation [4]. For instance, manufacturing the Cessna Denali aircraft engine using LPBF decreased the number of parts from 855 to 12, and increased fuel efficiency and power by over 10 percent [5].

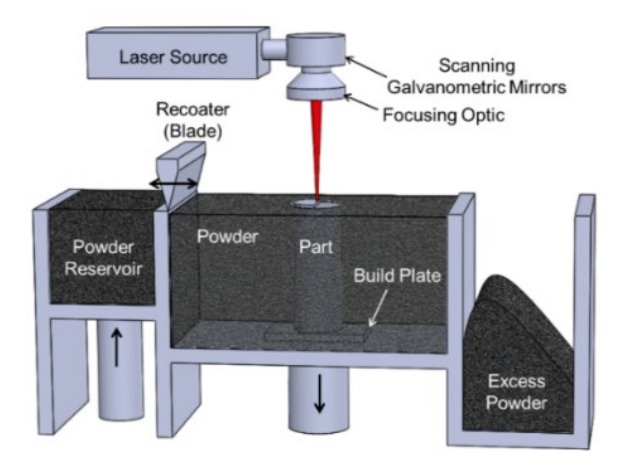


Figure 1: A schematic of the laser powder bed fusion (PBF-LB/M; LPBF) additive manufacturing process.

Despite its ability to reduce part count, eliminate intermediate manufacturing steps, decrease manufacturing lead time, and mitigate material waste, the use of LPBF parts for safety critical applications is currently hampered by flaw formation, e.g., inconsistencies in the microstructure, porosity, and distortion [1, 6]. These flaws, which range across multiple length scales cause uncertainty in the functional properties of a part, such as its strength and fatigue life, and require expensive and time-consuming post-process heat treatment to rectify [7, 8].

The spatiotemporal distribution of temperature, or thermal history, of a LPBF part as it is being built layer-upon-layer has a consequential effect on flaw formation and microstructure evolution [9-11]. The thermal history, in turn, is governed by complex interactions between material properties, part design, and 50+ processing parameters [12]. In this context, prior research has shown that apart from the processing parameters, such as laser power and scan speed, the part's design, build orientation, build layout, and placement of supports influence the thermal gradients and cooling rate during printing [13-15]. Therefore, a relatively small deviation in the build conditions can result in significant changes in the properties of a previously qualified part.

Currently, LPBF parts are qualified through extensive build-and-test empirical optimization on simple samples. These studies correlate processing parameters to porosity, microstructure evolution, and mechanical properties [16]. However, due to thermal history variations, these empirically optimized processing conditions seldom transfer successfully to complex geometries [17]. Hence, despite process optimization, there may be significant differences in microstructure between two different part geometries of the same material printed under identical processing conditions. Therefore, besides being prohibitively expensive to obtain, the empirically optimized parameters are specific to a part design and build layout and must be repeated for every new part design and layout [18].

Prior Work and Challenges

Flaw formation and microstructure evolution in LPBF parts are a result of thermal-fluid phenomena ranging across two scales, namely, meltpool- (< 100 μm) and part-scale (> 100 μm) 1.2 [19-21]. Understanding the interdependence and interaction of these multi-scale process phenomena and, subsequently, using this insight to predict microstructure evolved and functional properties remains an area of active research [22, 23].

At the micro-scale, the interface where the laser interacts with the powder is called the meltpool. The shape, size, and temperature distribution of the meltpool are linked to porosity, lack-of-fusion, microcracking, and instantaneous solidified microstructure [24-28]. Prior research has revealed that the meltpool temperature distribution and its morphology are mainly influenced by the processing parameters, such as laser power, velocity, laser spot size, hatch spacing, and to a smaller extent, the design of the part [29, 30].

At the macro-level part-scale, the thermal phenomena are related to the heat flux at the laser track level and across the scanned layers as the part is being built up. These thermal phenomena occur at a relatively slower time scale of tens of seconds compared to the micro-scale meltpool [10, 11]. As newer layers are deposited and melted, the preceding layers are reheated. The cyclical reheating is sufficient to cause the melting of the preceding two to five layers [31, 32]. The resulting part-scale thermal history is influenced by the processing parameters, part shape, orientation, supports, and other parts on the build plate [33]. A part shape with a gradual change in its geometric features is ideal for imparting a consistent thermal history in LPBF [34]. The part orientation with the presence of tall, slender, and overhanging features has been proven to cause inconsistencies in the resultant thermal gradients and the meltpool size, which in turn are detrimental to the microstructure evolution and mechanical properties of LPBF parts [35]. The

part-scale thermal history is also linked to thermal residual-stress-induced cracking and distortion, recoater crashes, and support failures [18, 33].

LPBF has been extensively applied to SS316L, an austenitic grade of stainless steel, preferred in aerospace and naval applications due to its high strength, toughness, and excellent corrosion resistance [36]. As shown in Figure 2, LPBF-processed SS316L parts exhibit a complex four-level hierarchical microstructure: solidified meltpool, grains, cell structures or dendrites, and twin boundaries [37, 38]. Meltpool boundaries are a fusion line between the previously solidified and newly melted material [39, 40]. The shape and size of the solidified meltpool, which is a primary determinant of the grain structure evolution in LPBF, depend on the processing parameters [41]. In face-centered cubic (FCC) crystal lattices, such as SS316L, relatively large thermal gradients across the build layers result in directionally solidified columnar grains and dendrites that grow epitaxially along the more favorable <001> direction [42, 43]. With sufficiently high thermal gradients and cooling rates typical to LPBF, these grains and dendrites can overlap several meltpools and form characteristic chevron patterns [23, 36, 44].

Dendrites consist of a cellular substructure separated by regions of high dislocation densities at these cell walls. Prior studies in LPBF of SS316L also reveal Cr-Ni-rich solute segregation at the cell boundaries [45]. Such a directionally solidified structure, coupled with the potential for flaw formation (e.g., porosity), induces a high degree of anisotropy in the mechanical properties of LPBF parts [46, 47]. In this context, researchers have exhaustively studied the influence of critical process parameters on microstructure evolution and functional properties [48-51]. Several studies have investigated the effect of the part build orientation on mechanical properties [38, 52]. It was observed that for transverse loading, where the loading direction is perpendicular to the length of the grains and parallel to the build layers, parts exhibit higher tensile

strength compared to longitudinal loading [38, 52]. This difference in mechanical performance is attributed to the orientation of columnar grains with respect to the loading direction, which also influences the fracture modes [53].

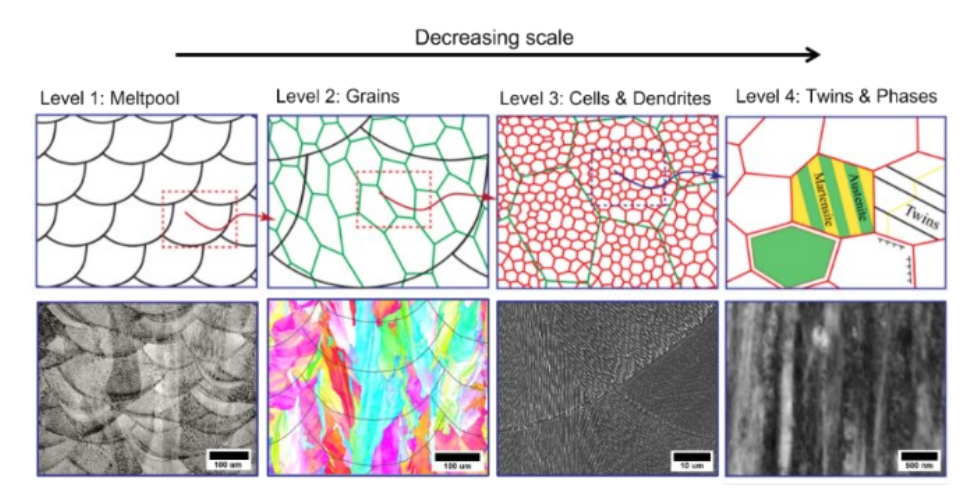


Figure 2. The four microstructure levels observed in LPBF-processed SS316L parts.

Summarized in Table 1 are select research papers that focus on exploring the process-structure-property relationships in LPBF of SS316L. For example, Agrawal *et al.* [49] experimentally determined a processing window for SS316L and provided a predictive model for hardness values and tensile strength as a function of input processing parameters. Wang *et al.* [54] and Yang *et al.* [55] developed finite element simulations to predict the effect of thermal history on microstructure evolution. Knapp *et al.* [23] explored the effect of the LPBF process to predict the microstructure heterogeneity in a part via meltpool scale thermal modeling and machine learning. However, in all of the preceding studies, the impact of only one processing condition was simulated. Hence, it is not possible to extrapolate the effect of several processing parameters on the thermal history and resulting microstructure and physical properties. The summary of the literature presented in Table 1 reveals a dearth of studies elucidating the *process-thermal history-microstructure-property* relationship in LPBF. This paper addresses the existing knowledge gap via experiments, computation modeling, materials characterization, and testing.

Table 1. Summary of literature comparing previous works on the process-structure-property relationship in LPBF of SS316L.

Ref.	Motivation	Conclusions	Characterization methods used	Modeling tools used
Agrawal et al. [49]	Rapid determination of processing window and effect of processing parameters on microstructure	Increasing energy density transforms finer grain structure to coarse elongated grains due to deeper meltpools and reduced cooling rates.	SEM, EBSD, Archimedes' density, Rockwell hardness	Predictive regression
Tekumalla et al. [46]	Effect of scan strategy on mechanical and hardness anisotropy	Orientation-dependent strengthening in <101> and <111> directions.	SEM, EBSD, Nanoindentation	Crystal plasticity constitutive model
Liu <i>et al</i> . [56]	Effect of scanning speed on microstructure and properties	Increasing scanning speed leads to a homogenous and finer grain structure but induces oversized and irregular lack-of-fusion pores. Tensile properties reduce slightly with decreasing scan speeds.	SEM, EBSD, Tensile testing, xCT, fracture surface analysis	None
Liu <i>et al</i> . [57]	Effect of laser power, exposure time, and build orientation on microstructure evolution and tensile properties	Increasing laser power and exposure time gradually changes the microstructure from fine equiaxed to coarse elongated grains, increasing keyhole porosity and lowering the strength.	SEM, EBSD, TEM, tensile testing, fracture surface analysis	None
Leicht et al. [58]	Effect of scan speed and hatch distance on microstructure, tensile strength, and build time.	Decreasing energy density altered the larger grains with <101> texture to smaller grains with random texture. Parts produced with lower energy density reduced the tensile strength by 5 % compared to the nominal condition.	Optical porosity imaging, SEM, EBSD, tensile testing.	None

Ref.	Motivation	Conclusions	Characterization methods used	Modeling tools used
Song <i>et al.</i> [59]	Effect of scanning strategies on the microstructure, grain growth, grain size, and, therefore, mechanical properties	Scanning strategy with a rotation angle impedes the epitaxial columnar growth and forms an equiaxial grain structure, which improves tensile strength and ductility.	SEM, EBSD, microhardness, tensile testing, fracture surface analysis	None
Wang et al. [54]	Effect of energy density induced thermal gradients on microstructure and mechanical properties	Due to layer-by-layer remelting, higher energy density leads to higher primary dendritic arm spacing (PDAS). Tensile strength increases until a threshold energy density is reached owing to the elimination of lack-offusion pores and then decreases because of excessively large PDAS.	Optical porosity imaging, SEM, XRD, tensile testing, microhardness	FEA simulation
Yang et al. [55]	Effect of LPBF processing on substructure formation and grain growth	Columnar dendritic grains grow epitaxially along the build direction, which is also the direction of heat flow. Cellular structure is formed due to high thermal gradients simulated at the meltpool scale.	SEM, EBSD, XRD	FEA simulation
Leicht et al. [60]	Effect of part thickness on microstructure and tensile properties	Tall and slender parts exhibited a unidirectional thermal gradient leading to preferential <101> orientation of the columnar grains and reduction in yield strength.	SEM, EBSD, XRD, tensile testing	None

Approach and Limitations

While previous research, as summarized in Sec.1.2, has correlated the effect of process parameters on defects, such as porosity, microstructure characteristics, and functional properties, e.g., the tensile strength of 316L, a key missing link remains in understanding the causal effect of the thermal history. The approach used in this work to address this extant gap in the LPBF literature is summarized below in Figure 3.

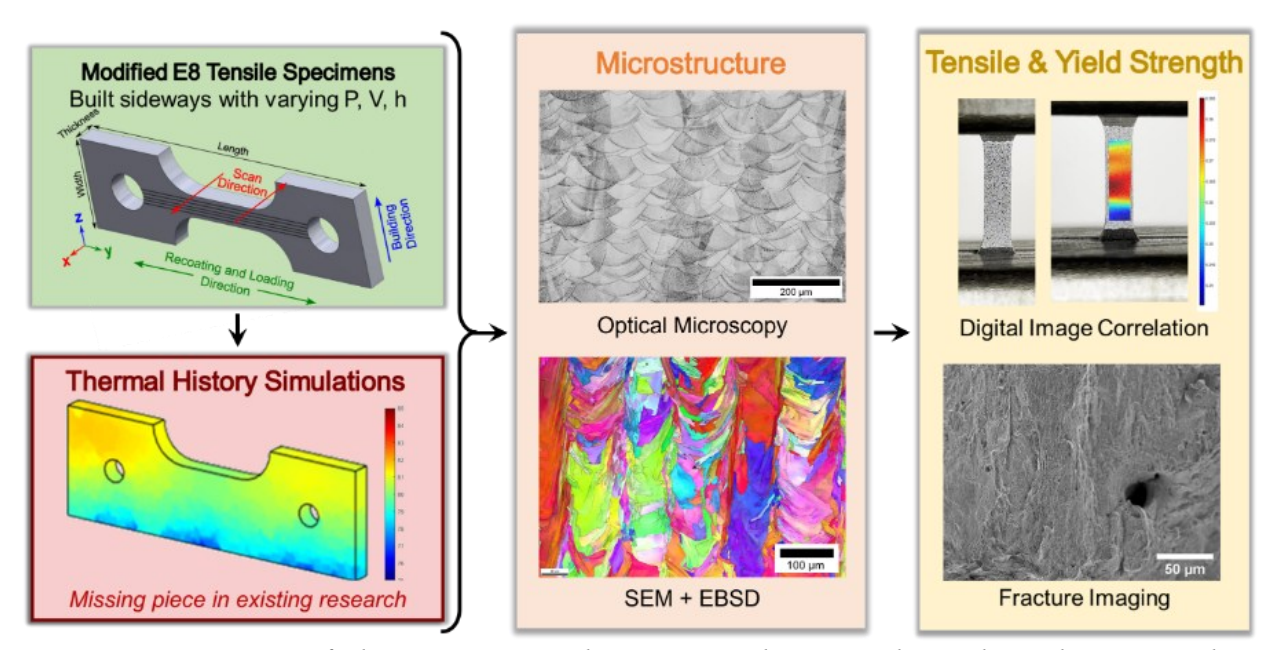


Figure 3. Summary of the computational-experimental approach used in this research to understand the process-thermal history-structure-property relationship in LPBF of SS316L.

Stainless steel 316L (SS316L) tensile samples were printed under four different processing conditions by varying laser power (P), velocity (V), and hatch spacing (H). Ten samples were printed under each of the four processing conditions, resulting in forty total samples. Porosity in the as-printed samples was non-destructively quantified using X-ray computed tomography. Subsequently, the samples were cross-sectioned and characterized using optical and scanning electron microscopy (SEM) to evaluate the microstructure, followed by electron backscatter diffraction (EBSD) to ascertain texture and orientation, and X-ray diffraction to identify the phases

present. Further, hardness measurements were obtained, and tensile testing was conducted with digital image correlation to measure the yield and ultimate tensile strength. A qualitative analysis of the fracture surface followed the tensile tests.

In parallel, the thermal history of each sample printed under the four processing conditions was predicted using an experimentally validated part-scale thermal simulation model detailed in our previously published works [18, 33, 61, 62]. From these simulations, two part-scale thermal history-related features were extracted, namely, (i) layer-wise end-of-cycle temperature (T_e); and (ii) layer-wise cooling time (t_c), analogous to the cooling rate (t_r). These quantifiers were subsequently correlated with the meltpool shape, grain morphology, texture, orientation, and mechanical properties of the tensile samples.

The main limitation of this work is that it only correlates but does not predict the effect of process parameters and part-level thermal history on the microstructure evolved. This limitation in the scope is because, to predict microstructure evolved in LPBF, it is essential to capture both the part-scale and meltpool-scale thermal-fluid phenomena [54, 63]. The latter is computationally demanding, with a few layers requiring several hours, if not days, on a supercomputer [23]. This shortcoming will be addressed in our future follow-up work through multi-scale meltpool and part-scale process modeling.

The rest of this paper is organized as follows: Sec. 2 describes the experimental procedure, sample characterization, and thermal modeling aspects. Sec. 3 reports the results concerning the effect of processing conditions on thermal history on microstructure evolution and mechanical properties. Finally, conclusions and avenues for future work are summarized in Sec. 4.

Methods

Experiments

Stainless steel 316L (SS316L) parts were manufactured on an EOS M290 LPBF system.

2. The gas atomized SS316L powder feedstock was sourced from Oerlikon with a D₁₀ of 15 μm and a D₉₀ of 45 μm. Consequential processing conditions are reported in Table 2. As shown in Figure 4(a) and (b), 40 tensile test coupons were printed under four sets of processing parameter combinations with varying combinations of laser power (*P*, [W]), scan speed (*V*, [mm·s⁻¹]), and hatch spacing (*H*, mm) settings. The processing conditions, labeled S1-S4, are reported in Table 3. Ten parts were printed under each processing condition.

Table 2: Processing conditions used to fabricate the LPBF parts used in this study, nominal process parameters, and materials characteristics of the metal powder.

Process Parameter [Units]	Values
Laser type, wavelength, and power.	Ytterbium fiber, 1070 nm wavelength continuous
	mode with 400 W max power
Nominal Laser Power (P) [W]	200
Nominal Scanning Velocity (V) [mm·s ⁻¹]	1100
Nominal Hatch spacing (<i>H</i>) [mm]	0.09
Layer thickness (<i>L</i>) [mm]	0.02
Stripes overlap [mm]	0.05
Stripe width [mm]	10
Nominal Volumetric global energy density	100
(E_{ν}) [J·mm ⁻³]	
Laser spot size [µm]	70
Scanning strategy	Bi-directional with no layer rotation
Build atmosphere	Argon
Build plate Preheat temperature [°C]	70
Recoater Cycle Time [sec]	10
Powder Material Properties	
Powder material type	SS316L
Powder particle size distribution [µm]	15 – 45 (D10 – D90)

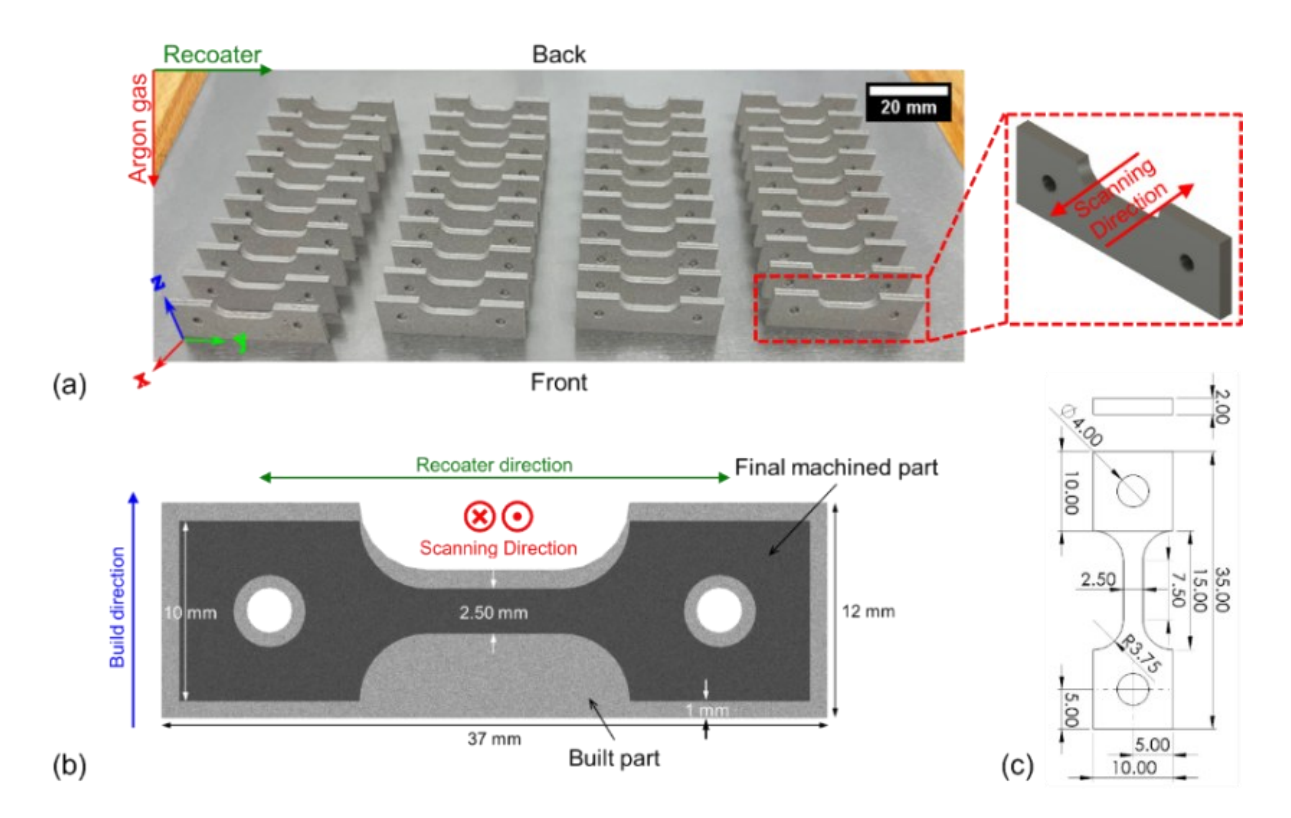


Figure 4: (a) Build plate with 40 tensile test samples (CAD model in the inset) built under varying processing conditions. The geometries show the parts with offset dimensions and support for the gauge section added as a solid geometry at the base, (b) a CAD model with 1 mm offset on all dimensions and a support structure for the gauge section (grey part), and the final tensile samples cut out (black part), (c) A schematic drawing of the final dimensions (in mm) of the tensile samples.

The rationale for selecting the treatment conditions in Table 3 is as follows: S2 is the nominal condition recommended by EOS with a volumetric energy density $E_v \sim 100 \text{ J} \cdot \text{mm}^{-3}$. The energy density $E_v = \frac{P}{V \cdot H \cdot L}$ is a function of laser power (P, [W]), scan speed $(V, [\text{mm} \cdot \text{s}^{-1}])$, hatch spacing (H, [mm]), and layer thickness $(L = 20 \text{ }\mu\text{m})$. Treatment condition S1 involves increasing the energy density by 25% from the nominal to $E_v \sim 125 \text{ J} \cdot \text{mm}^{-3}$. This increase in energy density is likely to result in keyhole-mode porosity [57, 64]. Treatment condition S4 represents an approximately 25% decrease in the energy density from the nominal to $E_v \sim 73 \text{ J} \cdot \text{mm}^{-3}$; the lower energy density is likely to cause poor consolidation of layers and lack-of-fusion pores [49]. Treatment condition S3 varies both the laser power and hatch spacing, with $E_v \sim 91 \text{ J} \cdot \text{mm}^{-3}$.

Table 3. Processing parameters used for sets S1-S4; S2 is the nominal processing condition of the LPBF machine.

Processing condition	Laser power (P) [W]	Scan speed (V) [mm·s ⁻¹]	Hatch spacing (H)[mm]	Energy Density $(E_v = \frac{P}{V \cdot H \cdot L})$ $[J \cdot mm^{-3}] (ca.)$
S1	225	1000	0.090	125
S2 (Nominal)	200	1100	0.090	100
S3	150	1100	0.075	91
S4	175	1200	0.100	73

The location of all 40 printed tensile samples was randomized on the build plate. The parts were staggered along the short axis (y-axis) to minimize recoater load and interaction between parts. The inert Argon gas flow is along the x-axis of the machine. Each as-printed test sample has dimensions, as shown in Figure 4(b). Solid support material was added under the gauge section of the samples to avoid deleterious effects, such as distortion. The as-printed parts were subsequently removed from the build plate and post-processed to the final dimensions with electro-discharge machining. The final dimensions are similar to the modified ASTM E8 tensile samples, as shown in Figure 4(c). This scaled-down geometry was chosen in order to accommodate all the samples on a single build plate. The critical gauge section of the finished samples was inspected to ensure the absence of burrs and other artifacts.

As depicted in Figure 4(a), tensile specimens were printed in the YX orientation, according to ISO/ASTM 52900:2021 convention, to align the gauge length with the expected tensile loading direction [65]. This orientation is preferred in the literature, as it provides enhanced functional properties (tensile and yield strength) compared to other configurations [38, 52]. A bidirectional/zigzag laser scan strategy along the x-direction was used with no layer rotation, and the build plate was preheated to 70 °C. Under these conditions, each part consisted of 600 layers, and the entire build was completed in 9 hours.

Materials Characterization

Non-destructive porosity analysis of one representative sample from each processing condition was conducted using X-ray computed tomography (X-ray CT, NorthStart Imaging X3000) at a voxel resolution of ~14 µm. Subsequently, samples were characterized using optical microscopy (OM) and scanning electron microscopy (SEM) to examine the grain structure and meltpool morphology, X-ray diffraction (XRD) to identify the phases present, and electron backscatter diffraction (EBSD) to characterize the grain size, texture, and morphology. These characterization measurements were performed in the gauge section, at approximately half the gauge length and at the midpoint of the width of the gauge section. The XRD analyses confirmed the presence of a single austenitic phase; the XRD results are reported in Appendix II.

A total of four samples (one each for S1-S4) were prepared for OM and SEM (JEOL IT-500HR) by grinding (300 to 1200 grit size) and polishing (6 μm and 1 μm diamond suspension and 0.05 μm colloidal silica) followed by etching with aqua regia (3: 1 = HCl: HNO₃) for 4 – 5 min. For sample preparation prior to EBSD, vibratory polishing was performed for six hours in 0.02 μm colloidal silica suspension. The crystallographic orientation and grain sizes of the printed samples were investigated by EBSD using a FEI Helios 600 NanoLab SEM with an EDAX Hikari camera, and the indexed data was processed using EDAX OIM Analysis software.

Mechanical Testing – Tensile Testing, Fracture Analysis, and Microhardness

Three samples for each processing condition were subjected to tensile loading at a strain rate of 0.5 min⁻¹ in displacement control. To quantify the strain evolution during these tests, the digital image correlation (DIC) technique is employed, wherein a black-on-white speckle pattern is overlaid onto the gauge length of the sample. Images of this speckle pattern were acquired at a rate of 1 frame per second, and a full field deformation was generated by processing these images

in MATLAB. The strain data is reported in the form of a stress-strain curve. The fractured surfaces of the tensile samples were cleaned with isopropanol and examined with SEM. Lastly, Vickers microhardness measurements were performed using a LECO LM110AT Hardness Tester at 0.1 N load at a dwell of 10 s, i.e., HV_{0.1/10}. A total of 15 microhardness measurements were obtained at random locations on the gauge section of the tensile samples.

Thermal Modeling

2.4.1 Background

2.4

The LPBF part geometry, processing parameters and material used, significantly affect the temperature distribution and cooling rates, and consequently, the microstructure evolved [66]. For predicting the part-scale temperature distribution T(x, y, z, t), it is necessary to solve the heat diffusion equation, Eq. (1) [67].

Material Properties
$$\frac{\partial T(x,y,z,t)}{\partial t} - k \underbrace{\left(\frac{\partial^2}{\partial x^2} + \frac{\partial^2}{\partial y^2} + \frac{\partial^2}{\partial z^2}\right)}_{Shape of the Part} \underbrace{\left(\frac{\partial^2}{\partial x^2} + \frac{\partial^2}{\partial z^2}\right)}_{T(x,y,z,t)} = Q$$
(1)

In this heat diffusion equation, material properties are assumed constant, where, ρ is the bulk material density [kg·m⁻³]; c_p is the specific heat capacity [J·kg⁻¹·K⁻¹]; k is the thermal conductivity [J·s⁻¹·m⁻¹·K⁻¹]; Q is the heat input per second required to melt a unit volume of the material [J·m⁻³·s⁻¹], also termed as the volumetric heat flux. The processing parameters in LPBF, such as the laser power (P, [W]), scan speed (V, [m·s⁻¹]), hatch spacing (H, [m]), layer thickness (L, [m]), and active laser time (t, [s]) influence the volumetric heat flux such that $Q = \frac{P}{V \cdot H \cdot L \cdot L}$.

Finite element-based (FE) thermomechanical analysis is the most commonly used approach in additive manufacturing to solve the heat diffusion equation, Eq. (1) [67]. The meshing of elements to mimic the evolving part geometry with each new hatch or layer being deposited

requires significant computational effort [62, 68, 69]. Specific commercial packages have reduced the computational burden of FE analysis using an adaptive meshing technique with part shape-based mesh refinement and coarsening [67, 70]. In adaptive meshing, the elements' size varies between time steps, which introduces uncertainty and adversely affects the prediction accuracy.

To overcome the challenges associated with the existing FE modeling, our prior works have experimentally validated a novel meshless thermal model based on graph theory [18, 33, 61, 62, 71]. This approach is summarized in Figure 5. Unlike FE-based analysis, graph theory does not employ matrix inversion to solve the heat diffusion equation, which vastly reduces the computational time without sacrificing accuracy [61]. Using the graph theory model, thermal gradients and cooling rates for each condition in this work were estimated in less than 5 minutes. The graph theory approach solves a discrete version of the heat diffusion equation. Consequently, a semi-analytical solution is obtained, resulting in Eq. (2).

$$T(x, y, z, t) = \Phi e^{-\frac{k}{\rho c_p} \Lambda t} \Phi' \left(\frac{A_e S_l}{\rho v c_n} \frac{P}{V} + T_{prev} \right)$$
 (2)

A set of discretized nodes is created to represent the part geometry. The temperature distribution, T(x, y, z, t) in Eq. (2) is solved as a function of the eigenvalues (Λ) and eigenvectors (φ) of the Laplacian Matrix (L) mapped over the discrete nodes.

In Eq. (2), A_e is the effective laser absorptivity, S_l is the total length scanned per layer, P [W] is the laser power, V [mm·s·l] is the scan speed, v [mm³] is the volume of melted material per layer, and T_{prev} [°C] is the temperature of the previously deposited layer (from simulation). In this work, $A_e = 0.60$ based on experiments by Ye *et al.* at Lawrence Livermore National Laboratory [72]. The advantage of using the graph theory approach, apart from its computational efficiency,

is that, unlike commercial simulation software, it preserves the temperature and cooling rate at each point under the sub-surface.

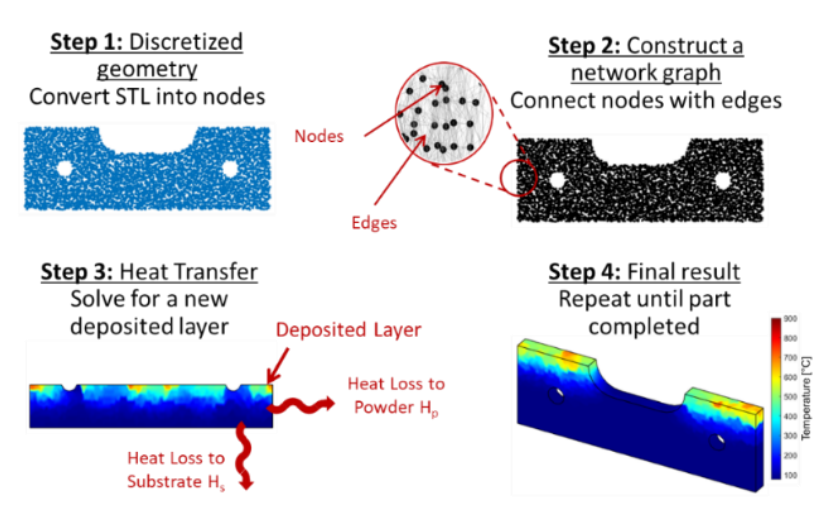


Figure 5. A schematic representation of the mesh-free graph theory modeling approach used in this study to simulate the thermal history of tensile samples processed by LPBF.

The graph theory model is based on the following assumptions and limitations [18, 33, 61, 62, 73].

- The effect of latent heat on account of material phase changes from solid to liquid and back to solid is not considered.
- Material properties, such as specific heat and conductivity, are considered constant and not temperature-varying. In this work, the material properties at a temperature midway between the melting point and ambient temperature are used.
- To aid computational efficiency, a selection of the entire layer(s) is assumed to be deposited instantaneously, called the super-layer or meta-layer approach, viz., also a common assumption in part-level modeling with FE-based models [69].

Despite these assumptions, as shown in several of our previous works, the graph theory approach predicts the part-level temperature distribution with an error of less than 5% and an order of magnitude faster than FE-based models [61, 62]. Experimental validation of the model in the context of a complex practical geometry is detailed in Appendix I.

2.4.2 Model-derived thermal gradient and cooling rate metrics

Figure 6 is a representative temperature-time curve obtained from the nominal treatment condition S2 using the graph theory approach. A steep increase in temperature is observed at the instant of the laser strike. Almost instantaneously following the laser strike, the temperature of the material increases above the liquidous temperature of T_{liq} ~ 1440 °C, followed by a relatively gradual cooling. The material solidification kinetics occurs below the liquidous temperature. The fast cooling rates inherent to LPBF result in single austenitic phase formation in SS316L, which was confirmed through XRD phase analysis in Appendix II. Further, below the upper critical temperature (A_{c3}) of 723 °C, no material phase change is involved in SS316L, and all the liquid solution completely solidifies below this temperature. Therefore, the rationale is to quantify the part temperature distribution and cooling times between the temperatures of 1600°C and 700 °C, a range where all the solidification kinetics occur.

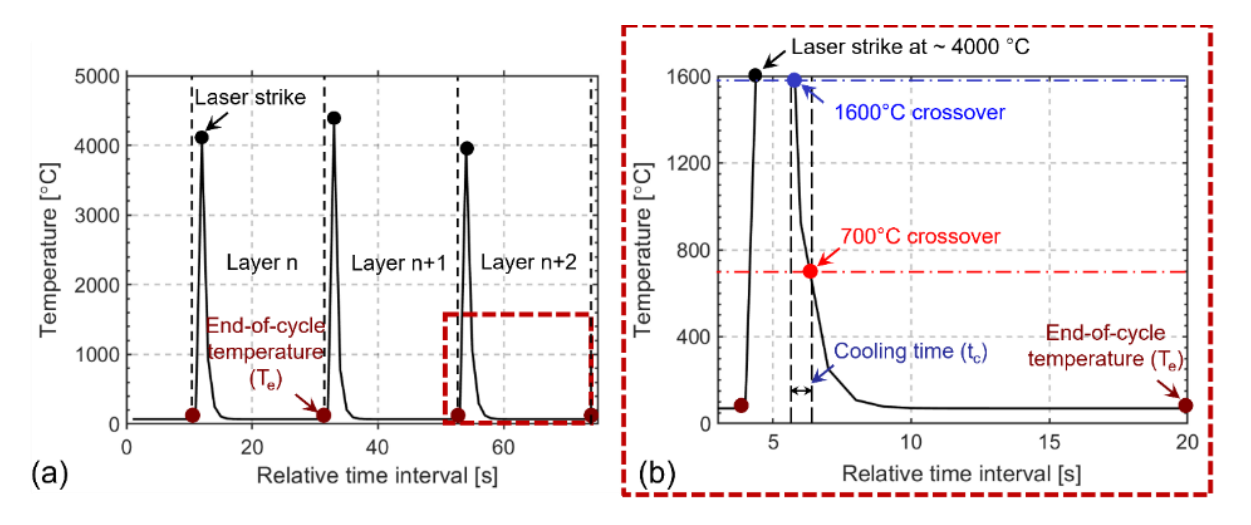


Figure 6. Schematic showing the representative thermal cycling (a) over three-layer scans as a result of the laser strike and a subsequent cool-down period, (b) Over an individual laser scan in the LPBF process, this work estimates the cooling time - (t_c) for a layer to cool down from 1600 °C to 700 °C and the end of cycle temperature - (T_e).

Accordingly, two thermal metrics from the simulation-derived temperature-time cooling curves are extracted, as shown in Figure 6(b). The first is the end-of-cycle temperature (T_e , [°C]), which is the average surface temperature of a layer after a fresh layer of powder is deposited on top. End-of-cycle temperature (T_e) is an analogue to the spatial thermal gradient aspect of the part-level thermal history. The second metric is the cooling time (t_c), which is the time required to cool from 1600 °C to 700 °C. The cooling rate t_r is closely related to t_c ; it is defined as $t_r = \frac{1600 \, ^{\circ}C - 700 \, ^{\circ}C}{t_c}$ [°C·s⁻¹]. In this work, these thermal history metrics T_e , t_c , and t_r , are estimated specifically for the gage section within the tensile samples, since the microstructure in this is consequential to the mechanical properties. Consequently, the effect of thermal history on microstructure heterogeneity elsewhere can be discounted.

The use of end-of-cycle temperature (T_e), cooling time (t_c), and cooling rate (t_r) as thermal history metrics to correlate with microstructure evolution is justified as follows. A solidification map, called the G vs R curve, has been extensively used in welding and more recently in the context of metal additive manufacturing to explain the microstructure evolved [30, 74, 75]. The key factors governing the evolution of solidification structure in metal additive manufacturing are the temperature gradient (G, [°C·m⁻¹]) and the solidification rate (R, [m·s⁻¹]) [74]. The metrics G/R [°C·s m⁻²] and $G\times R$ [°C·s⁻¹] are correlated to the type and size of the grains. The G/R ratio determines whether the solidified microstructure is planar, cellular, dendritic, or equiaxed. Whereas the $G\times R$ metric determines whether the grain structure is coarser or finer. A higher $G\times R$ leads to a fine grain structure, i.e., smaller grain size and primary dendritic arm spacing [63]

However, precise prediction of G and R for the entire part is computationally expensive as it requires multi-scale modeling, encompassing meltpool-level and part-scale thermal phenomena [25]. Part-scale simulations discount localized melting of the powders, resulting in a phase change

from solid to liquid and back to solid [62]. Therefore, part-scale models, including the graph theory approach used in this work, cannot precisely estimate G and R.

Instead, this work considers the part-scale cooling rate (t_r) and end-of-cycle temperatures (T_e) obtained from the graph theory thermal simulations as being analogous to R and G, respectively. This analogy was motivated by our recently published work, Ref. [71], where we used t_r and T_e estimated from the graph theory model in place of R and G to predict the primary dendritic arm spacing in LPBF of Inconel 718. In Ref. [71] we used these graph theory-derived thermal history metrics were employed as inputs to a machine learning model trained to predict the primary dendritic arm spacing with accuracy exceeding 80% (statistical F1-score). It is noted that the microstructures of LPBF- processed Inconel 718 characterized in Ref. [71] depict similar epitaxial dendritic-type grains to those of Stainless Steel 316L from this work.

Results

Effect of Processing Conditions on Thermal History

Figure 7 depicts a transient snapshot of the predicted temperature distribution for select 3.

3.1 layers of for treatment conditions S1-S4. For the highest energy density levels of S1 ($E_v \sim 125$ J·mm⁻³) and S2 ($E_v \sim 100$ J·mm⁻³), as shown in Figure 7(a) and (b), respectively, the sub-surface layers are at a higher temperature compared to S3 ($E_v \sim 91$ J·mm⁻³) and S4 ($E_v \sim 73$ J·mm⁻³). In other words, higher levels of energy density result in more significant heat buildup and larger temperature gradients.

In Figure 7 local heat retention regions (hot spots) are observed at layer 350 (7 mm). Hot spots are prominent on the edges (boundary nodes) and around the holes incorporated in the geometry of the tensile samples. The edges around these holes act as the overhanging regions during the LPBF, leading to higher heat retention. Since Figure 7 is a transient snapshot taken at an instance of 0.5 seconds after deposition of a layer, these hotspots subsequently cool down.

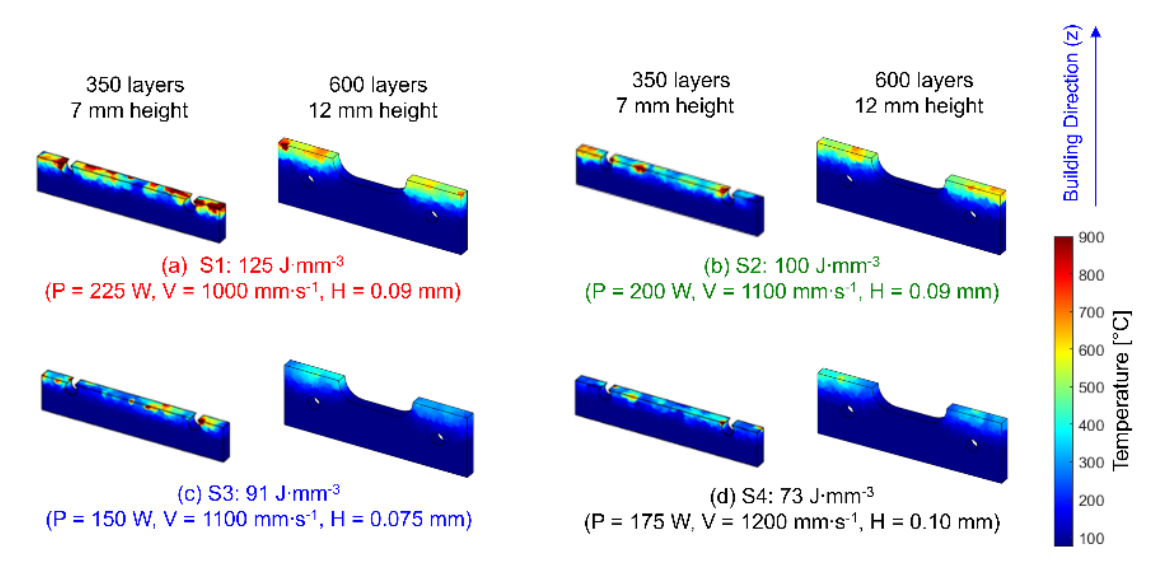


Figure 7. Visual representation of thermal gradients in treatment conditions (a) S1, (b) S2, (c) S3, and (d) S4 for layers 350 and 600. Temperatures depicted here are at a time step of 0.5 seconds after the laser strikes the top surface. The thermal gradient increases with increasing energy density.

The effect of the four processing conditions S1-S4 on the end-of-cycle temperature (T_e) and cooling times (t_c), are observed in Figure 8 (a) and (b), respectively. Increasing the energy density from S4 to S1 increases both T_e and t_c . Referring to Figure 8 (a), the higher energy density of treatment conditions S1 and S2 compared to S3 and S4 will result in higher heat retention in part during the build, and hence T_e is relatively larger. In Figure 8 (a), the end-of-cycle surface temperature T_e increases as new material is deposited layer-by-layer. After 4 mm of build height (200 layers), T_e progressively increases in magnitude for all four treatment conditions. Further, T_e increases sharply between the build heights of 6 to 7.5 mm (layers 300 to 450). The top half of the holes (seen from the geometry of the tensile samples in Figure 4(b)) are being printed within these layers. These holes subsequently act as the overhanging features leading to this steep rise in end-of-cycle temperatures. This observation further corroborates the localized hotspots in layer 350 of the simulation snapshot shown in Figure 7.

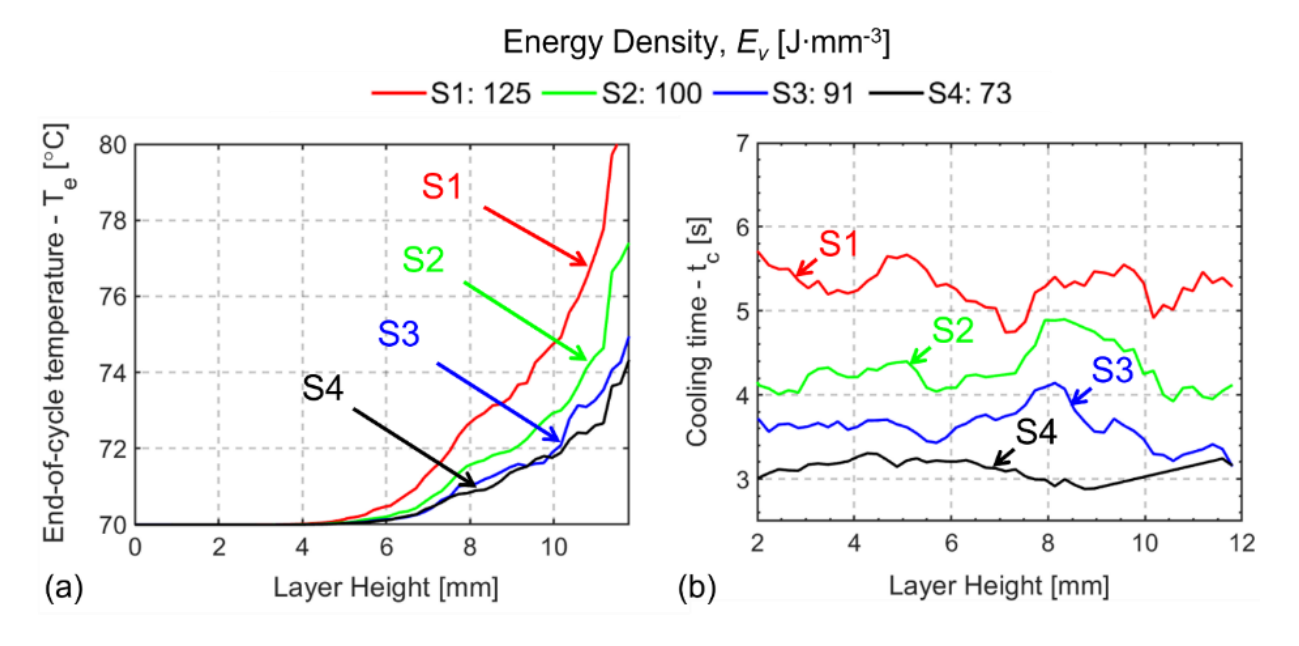


Figure 8. (a) End-of-cycle (surface) temperature $-T_e$ and b) Average layer cooling time $-t_c$ (from 1609 °C to 700 °C) for each sample set predicted from the graph theory thermal model. T_e and t_c are both seen to be increasing with an increase in the energy density.

For this geometry, the increasing trend in T_e with layer height is explained as follows: as the part grows in the vertical direction, the distance of the active printing surface layer from the substrate increases. Thus, the heat sink effect of the substrate progressively diminishes, and input heat tends to be retained in the layers farther from the substrate. The T_e for S3 and S4 overlap owing to the complex interaction between processing parameters. Referring to Table 3, S3 has the lowest laser power (150 W) and narrowest hatch spacing (0.075 mm) among all the conditions. Whereas S4 has higher laser power (175 W) but the fastest scan speed (1200 mm·s⁻¹) and widest hatch spacing (0.1 mm).

Referring to Figure 8 (b), the increased energy density of S1 and S2 results in a deeper meltpool and increased volume of melted sub-surface layers. In comparison, at the lower energy density treatment conditions S3 and S4, the meltpool is shallower, and a lesser volume of sub-surface layers are melted. Since a larger molten mass will require a longer time to cool to a constant temperature, the cooling time (t_c) is longer (Figure 8 (b)), and the cooling rate (t_r) is slower at higher energy density levels concerned with treatment conditions S1 and S2, compared to the lower energy density treatment conditions S3 and S4.

Porosity

Summarized in Table 4 are XCT analysis results for S1-S4 in terms of the mean and standard deviation of pore sizes, number of pores, and volume fraction of porosity relative to the volume of the part to three significant digits. Apart from treatment condition S3, none of the tested samples showed porosity beyond two significant digits. The volume fraction porosity for S3 was $\sim 0.05\%$. These porosity-related results from XCT were subsequently verified with OM and SEM.

Table 4. Pore size distribution in processing conditions S1-S4 obtained from XCT analysis.

Processing Condition	Average pore sizes detected (µm) with standard deviation in the brackets	Number of pores detected	Volume fraction of defects in the XCT scanned parts
S1	$37.8 \ (\sigma = 23.6)$	46	0.001 %
S2 (Nominal)	$38.3 \ (\sigma = 26.1)$	196	0.004 %
S3	$52.5 (\sigma = 37.0)$	804	0.05 %
S4	No pores detected	No pores detected	0.000 %

Shown in Figure 9 are XCT, OM and SEM images obtained for a representative sample from processing condition S3. Referring to Figure 9, the energy density of S3 $(E_v \sim 91~\mathrm{J\cdot mm^{-3}})$ is higher than S4 $(E_v \sim 73~\mathrm{J\cdot mm^{-3}})$, however, the lower laser power of S3 $(P = 150~\mathrm{W})$ compared to S4 $(P = 175~\mathrm{W})$, was insufficient to melt the material resulting in lack-of-fusion porosity characterized by its jagged shape. As observed from the etched optical micrograph, the lack-of-fusion pores in S3 occur at the meltpool boundaries. These lack-of-fusion pores are detrimental to functional integrity as they are sites for local brittle fracture during tensile testing, resulting in reduced strength. The effect of porosity on the fracture mode is discussed in depth in Sec. 3.6.2.

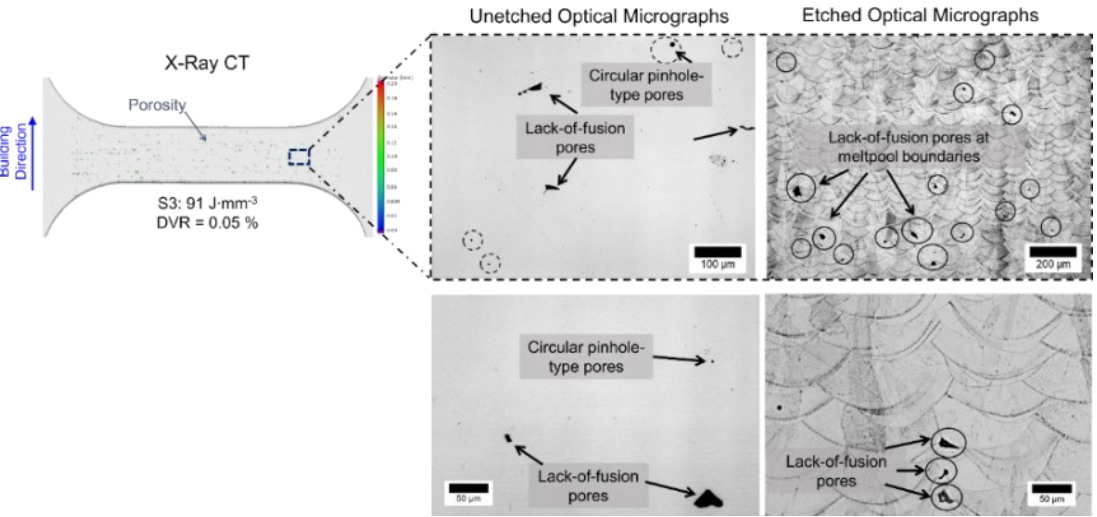


Figure 9. The defect volume ratio (DVR) for S3 shows the porosity levels in the gauge section of the final EDM cut dog bone. Optical micrographs show that these porosities correspond to lack-of-fusion pores. S3 shows a DVR of $0.05\,\%$ due to the lowest laser power, leading to lack-of-fusion pores. S1, S2, and S4 have a cumulative DVR of $0\,\%$ for pores larger than $28\mu m$ in these processing conditions.

Meltpool Morphology and Grain Type

Representative optical images for the four processing conditions S1-S4 are shown in Figure 10. These micrographs reveal the meltpool morphology typical to LPBF with prominent 3.3 boundaries formed by the laser scanning tracks. The optical micrograph in Figure 10(a) depicts that the microstructure of S1, is predominantly composed of columnar dendrites resulting from the rapid cooling rates inherent to LPBF. The columnar dendrites are observed to overlap multiple meltpool boundaries. These columnar dendrites solidify along the build direction and opposite to the direction of the heat flux, consistent with observations in literature [42, 49, 63, 74]. The crossover of columnar dendrites into adjacent meltpools also manifests in the corresponding SEM micrograph in Figure 11(a1). Further, in the zoomed-in image in Figure 11(a2), the columnar dendrites of S1 span several meltpool boundaries.

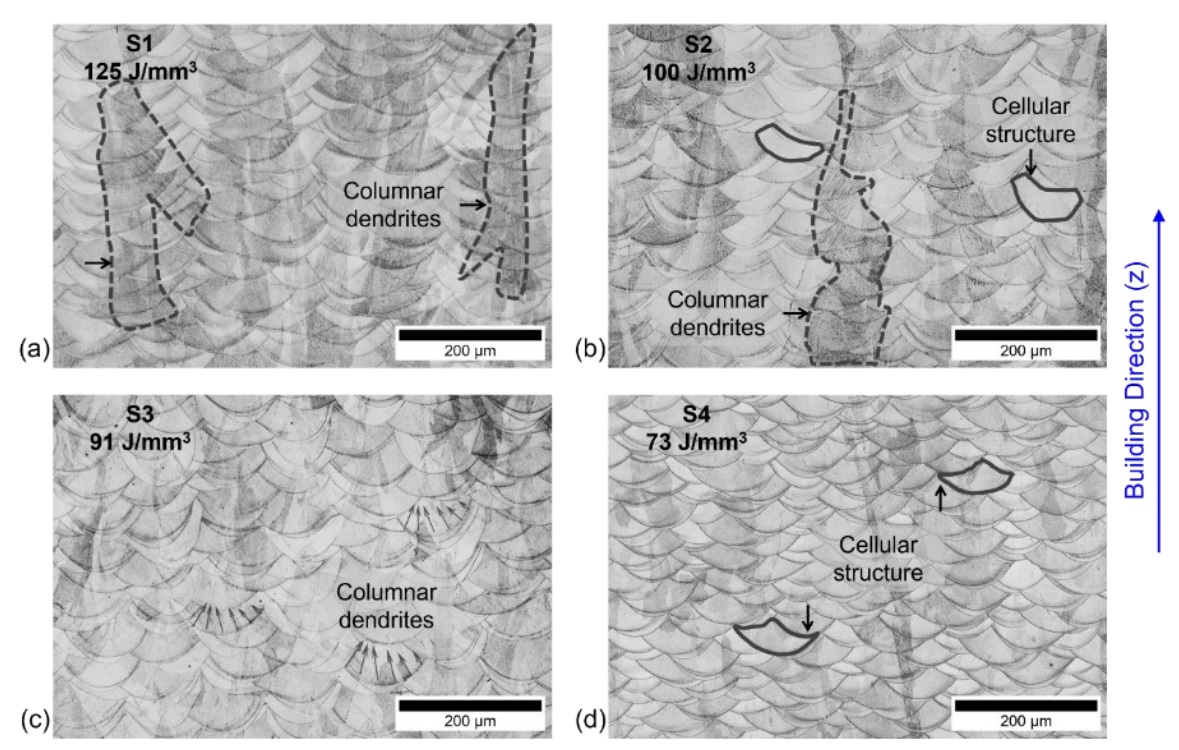


Figure 10. Optical micrographs for conditions S1-S4. The highest energy density in S1 shows a tendency of columnar dendrites to grow (dashed outline) across the meltpool boundaries and multiple build layers. The lowest energy density in S4 restrains the grain growth to the individual meltpools such that the meltpool boundaries (solid outline) are a well-defined feature.

The microstructure of S2 depicted in Figure 10(b) also consists of columnar grains (black dashed outlines) solidified along the build direction. As in S1, the columnar dendrites of S2 range across multiple meltpool boundaries. The SEM micrograph of S2 is highlighted in Figure 11(b1). A higher magnification image in Figure 11(b2) shows that the microstructure of S2 also consists of a fine cellular structure. While the columnar dendrites tend to grow along the build direction, the cross-sectional cellular structure has a relatively disordered growth direction. Examining the SEM micrographs in Figure 11(b2), the minority of fine cellular structures present in S2 are confined to the individual meltpool boundaries.

The cross-meltpool columnar grain growth observed both in S1 and S2 is explained in the context of Figure 8(a) and (b). The higher energy input of S1 and S2 results in higher end-of-cycle temperatures (T_e) and longer cooling times (t_c). The large energy density and resulting heat retention remelts a larger volume of the previously solidified layers, manifested in Figure 11(a) in the form of a relatively larger meltpool penetration. The re-melting of previous layers leads to epitaxial regrowth of columnar dendrites across the meltpool boundaries, and the high T_e and t_c contribute toward grain coarsening.

Thus, the SEM images of the meltpool shown in Figure 11 confirm the inferences from the optical micrographs from Figure 10. Comparing the meltpool profiles for various treatment conditions, demarcated from the white solid outlines of meltpool boundaries in Figure 11, S1 results in deeper and wider meltpool than S2. By contrast, S4 has the shallowest and narrowest meltpool compared to S1 and S2. In other words, the meltpool size is linked to the processing conditions and thermal gradients.

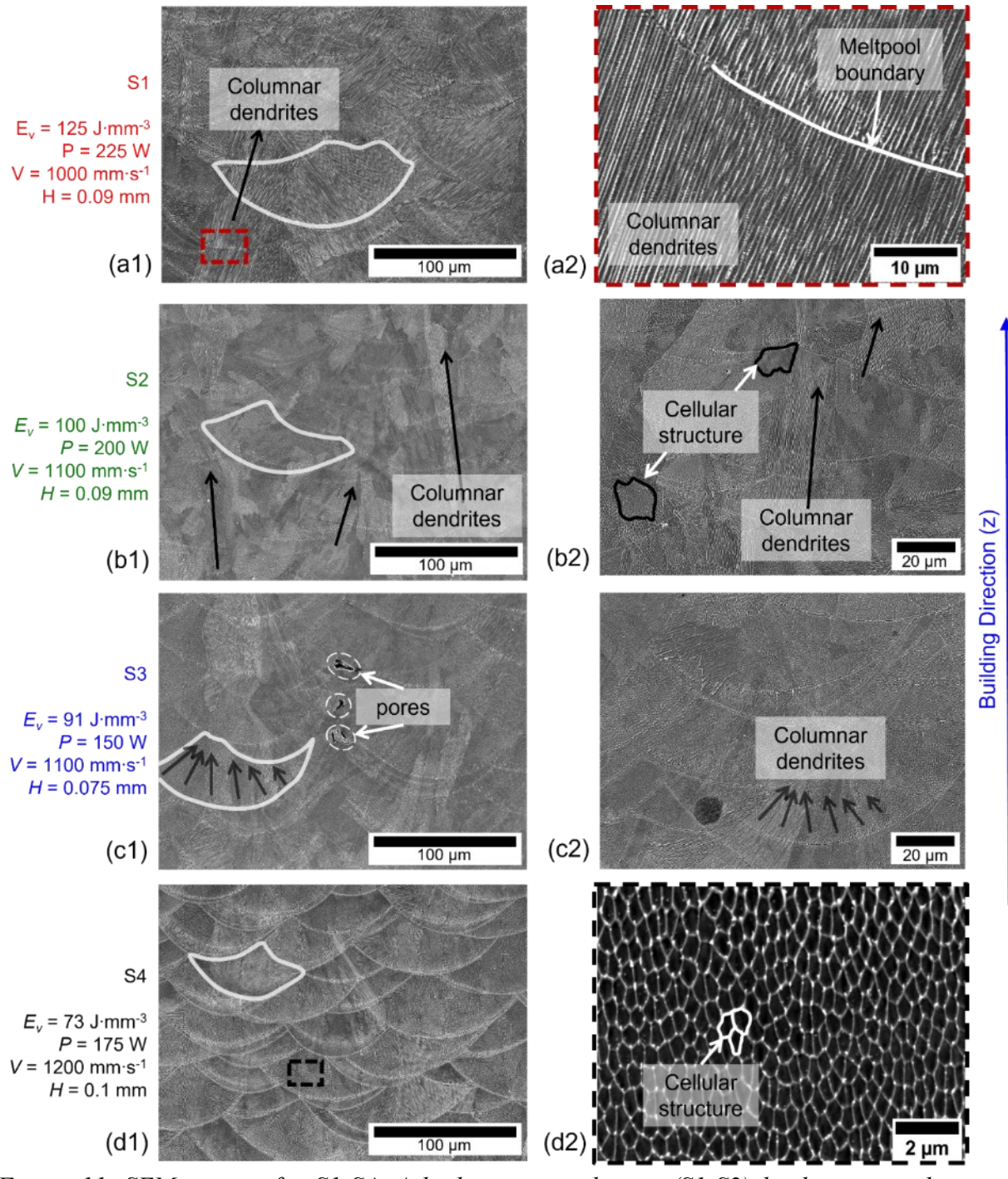


Figure 11. SEM images for S1-S4. A higher energy density (S1-S2) leads to a unidirectional columnar dendrite that grows epitaxially along the build direction. In contrast, a lower energy density (S3-S4) leads to localized clusters of a cellular structure because of randomly oriented equiaxed dendrites.

The SEM micrographs of S3 in Figure 11(c1) and (c2) further exemplify the presence of the columnar dendrites, albeit for a reduced length scale compared to S1 and S2. Unlike in S1 and S2, these columnar dendrites in S3 are restricted to individual meltpools, shown by the black arrows confined to the white solid meltpool outlines. The optical micrograph in Figure 10(c) also highlights the constricted columnar dendritic growth of S3. As discussed in Sec. 3.2, the porosity results point towards lack-of-fusion pores in S3. Further evidence for lack-of-fusion porosity is seen in Figure 11(c1). The white dashed outlines indicate to lack-of-fusion pores at the intersection of adjacent meltpools. Due to a lower laser power of S3, lack-of-fusion porosity is not eliminated by re-melting subsequent layers.

In contrast, as evident from Figure 11(d1) and (d2), the microstructure of S4, i.e., the lowest energy density tested at $E_v \sim 73 \text{ J} \cdot \text{mm}^{-3}$, consists predominantly of fine cellular structures, which, like S3, is also confined to individual meltpool boundaries. As explained in Figure 8, the lower magnitude of T_e and shorter t_c of S3 and S4 relative to S1 and S2 results in limited remelting of previously deposited layers. Hence, the epitaxial growth of the columnar dendrites across meltpool boundaries is restricted. Moreover, a faster scan speed has been linked with promoting a randomized cellular structure and an equiaxed nature of the grains [41, 76]. This, in addition to the lowest energy density used, restricts the heat transfer to within the meltpool boundaries in S3 and S4. Through the EBSD analysis in the following section, Sec. 3.4, the nature of the columnar dendrites, fine cellular structure, and their relationship with the underlying grain structure, as well as the part thermal history, will be explained.

Crystallography, Texture, and Phases

The EBSD orientation maps and the inverse pole figures (IPF) for the four-processing conditions S1-S4 are shown in Figure 12 and Figure 13, respectively. The microstructure evolved 3.4 along <100> texture corresponds to the presence of columnar dendrites; <101> texture to fine cellular structure; and <111> texture to the slanted columnar dendrites.

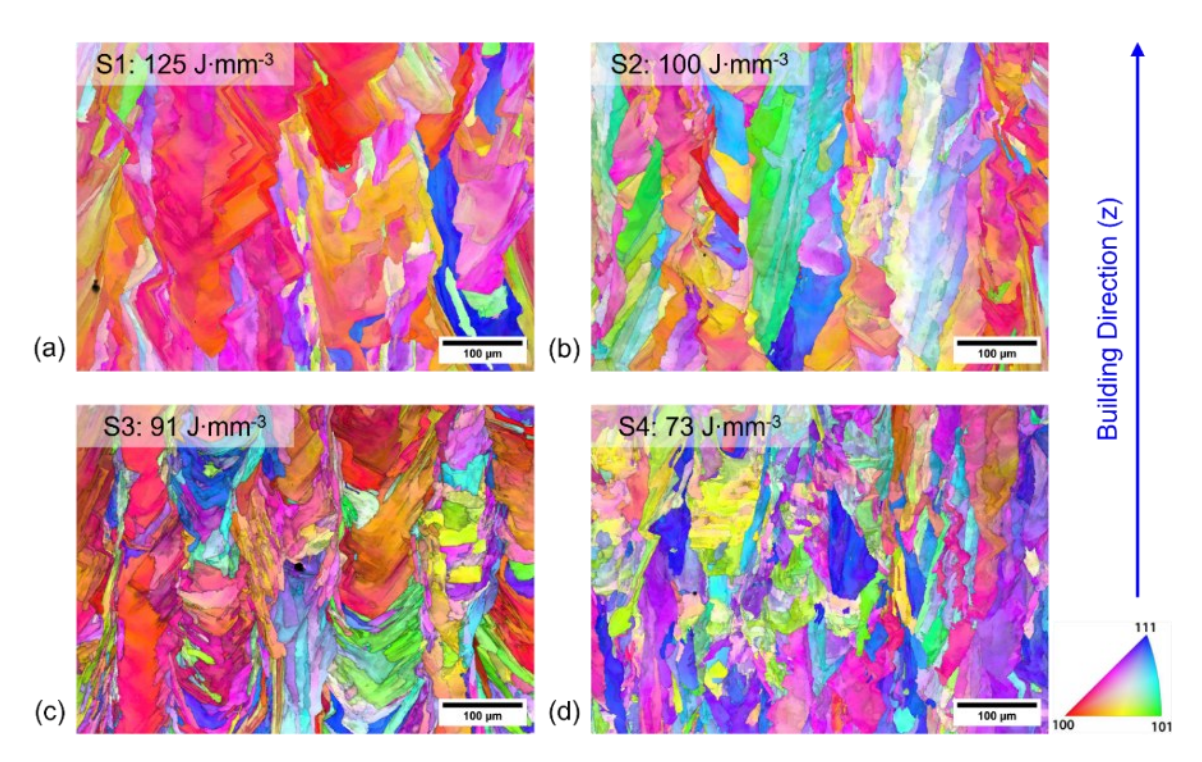


Figure 12. EBSD orientation maps of SS316L. The highest energy density condition S1 and S2 promote epitaxial grain growth overlapping multiple meltpool boundaries. In contrast, the lowest energy density S3 and S4 promotes equiaxed grain structure constricted to individual meltpools.

Consistent with the microstructure of S1 examined using OM and SEM in Figure 10(a) and Figure 11(a), respectively, the orientation map in Figure 12(a) reveals the presence of a columnar grain structure growing epitaxially along the build direction owing to the high energy density and laser power used for these samples. In the IPF from Figure 13 (a), S1 also shows a preference for the <100> texture along the build direction and a minor preference for <101> texture along the loading direction. As explained in the preceding section 3.3, the high energy density (E_v = 125)

J·mm⁻³) of S1 facilitates epitaxial columnar grain growth across multiple meltpool boundaries between layers, albeit there is local misorientation resulting in a vertical zigzag pattern seen in Figure 12(a).

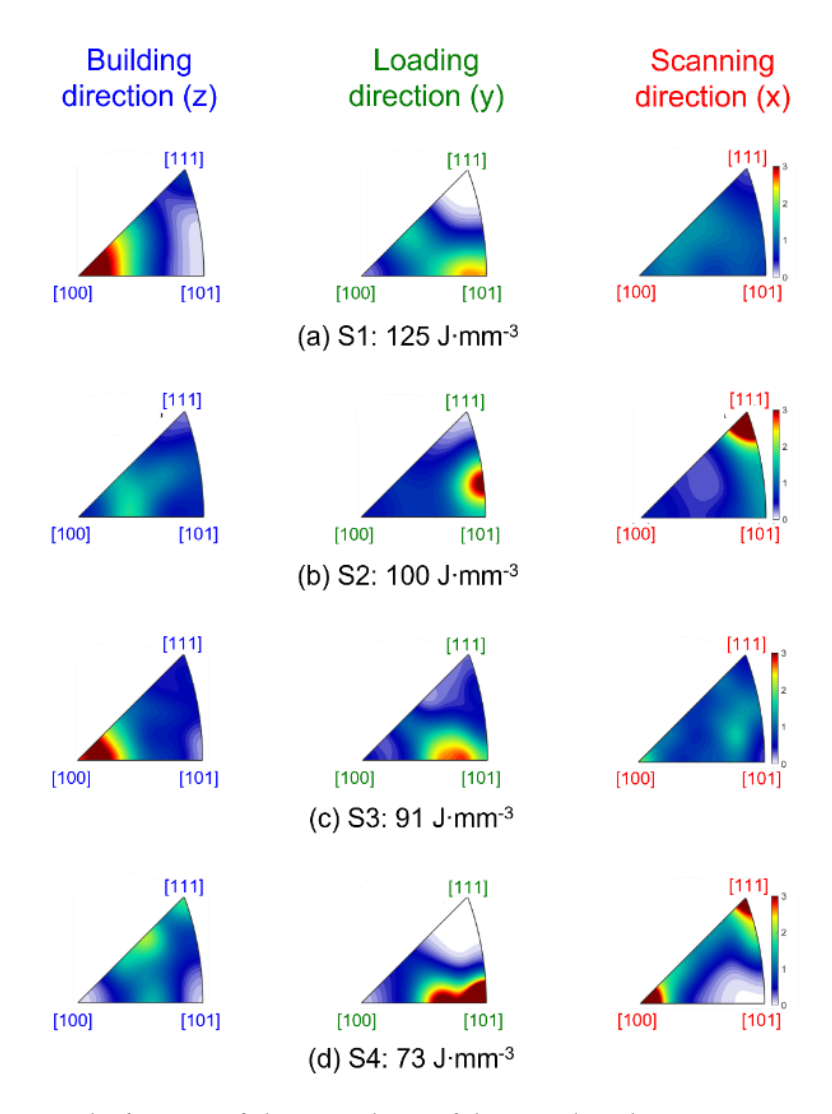


Figure 13. Inverse pole figures of the sample set fabricated with varying energy densities in the build direction (z), loading direction (y), and scanning directions (x) as reference axes.

For S2, while there is no discernible preference for grain growth orientation along the build direction (Figure 13(b)), there is a strong preference for growth along <101>, viz., the loading direction. Owing to the reduced energy density compared to S1, the grains of S2 are columnar and elongated but also marginally equiaxed, as evident from Figure 12(b). The IPF for S4 is shown in

Figure 13(d)), which indicates a lack of preference for grain orientations along the build direction. The lowest energy density in S4 also leads to the formation of a large proportion of equiaxed grains with <101> and <111> orientations.

There is a preferred <111> texture along the scanning direction for S2 (Figure 13(b)) and S4 (Figure 13(d)), which is not observed in S1 (Figure 13(a)) and S3 (Figure 13(c)). Such a texture along <111> direction in S2 and S4 results from the tilted dendritic growth with respect to the build direction. This is because, in addition to the thermal gradient along the build direction, faster scan speeds and lower laser power in these sets compared to S1 generate a thermal gradient along the scanning direction, which influences the solidification and local growth of the columnar grain structure within the layer. This, in turn, promotes dendrites to grow along a vector that follows both the build and scan directions, leading to a tilted solidification axis. Therefore, without a layer rotation, the thermal gradient is strongly influenced by the laser source intensity along the build direction and its scan path along the scanning direction S2 and S4.

Consistent with observations from optical images and SEM, the solidified grains in the previous layers do not regrow epitaxially due to the lower energy density and laser power in S3 and S4. This leads to a relatively equiaxed grain structure of S3 and S4 in meltpool boundary regions between two subsequent scanning tracks farthest from the center of the laser spot.

A comparison of the average grain sizes and the average primary dendritic arm spacing (PDAS, λ_1) is provided in Figure 14. The PDAS is estimated from SEM images by calculating the cell area from 20 high-magnification images for each processing condition. Figure 15(a-d) shows the empirical grain size distribution measured from the EBSD orientation maps corresponding to treatment conditions S1-S4 (Figure 12). Grain sizes estimated herein are the cumulative averages of the length of major and minor axes of individual grains measured from EBSD. As evident from

Figure 14, both grain size and PDAS have similar trends; they are proportional to energy density (E_v) . This is because, as explained in the context of Sec. 3.1, the end-of-cycle temperature (T_e) and cooling time (t_c) increase proportionally to heat accumulation (Figure 8), noting that cooling time is inverse of the cooling rates.

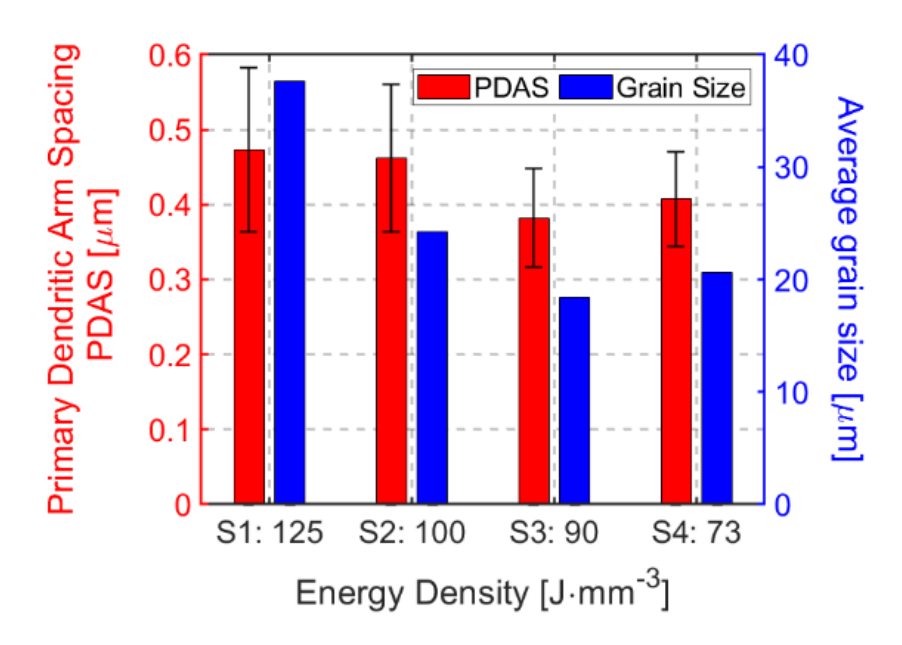


Figure 14. PDAS and average grain size for treatment conditions S1-S4; these are proportional to energy density.

Referring to Figure 15, samples made under treatment condition S1 have an average grain size of 37 μ m (σ = 62.3 μ m); 82.5 % of grains indexed were smaller than 50 μ m and 8.8 % columnar grains larger than 100 μ m with the largest grain size of 357 μ m. Similarly, in S2, the average grain size in the gage section is 24 μ m (σ = 38.6 μ m), with 4.2 % grains larger than 100 μ m owing to the presence of columnar grains extending across multiple meltpool boundaries between layers. However, 87.5 % of grains in S2 are smaller than 50 μ m, which is higher compared to S1 due to fine-sized equiaxed grains.

Samples processed under treatment condition S3 result in a smaller average grain size of $18 \mu m$ ($\sigma = 25.3 \mu m$) due to the presence of lath-like fine columnar grains with 94.4 % grains

smaller than 50 μ m. These lath-like grains form a horizontal chevron pattern observed in Figure 12(c). Additionally, S3 has a smaller primary dendritic arm spacing (λ_1) compared to S1 and S2 due to low thermal gradients and rapid cooling. However, the smallest grain size seen in S3 results from a fine elongated columnar grain structure leading to a lath-like grain morphology; S3 also has 2.3 % grains larger than 100 μ m compared to 1.3 % in S4. Samples processed under treatment condition S4 have an average grain size of 20 μ m (σ = 30.6 μ m), and the grain size distribution is similar to S3 due to the equiaxed nature of the grains.

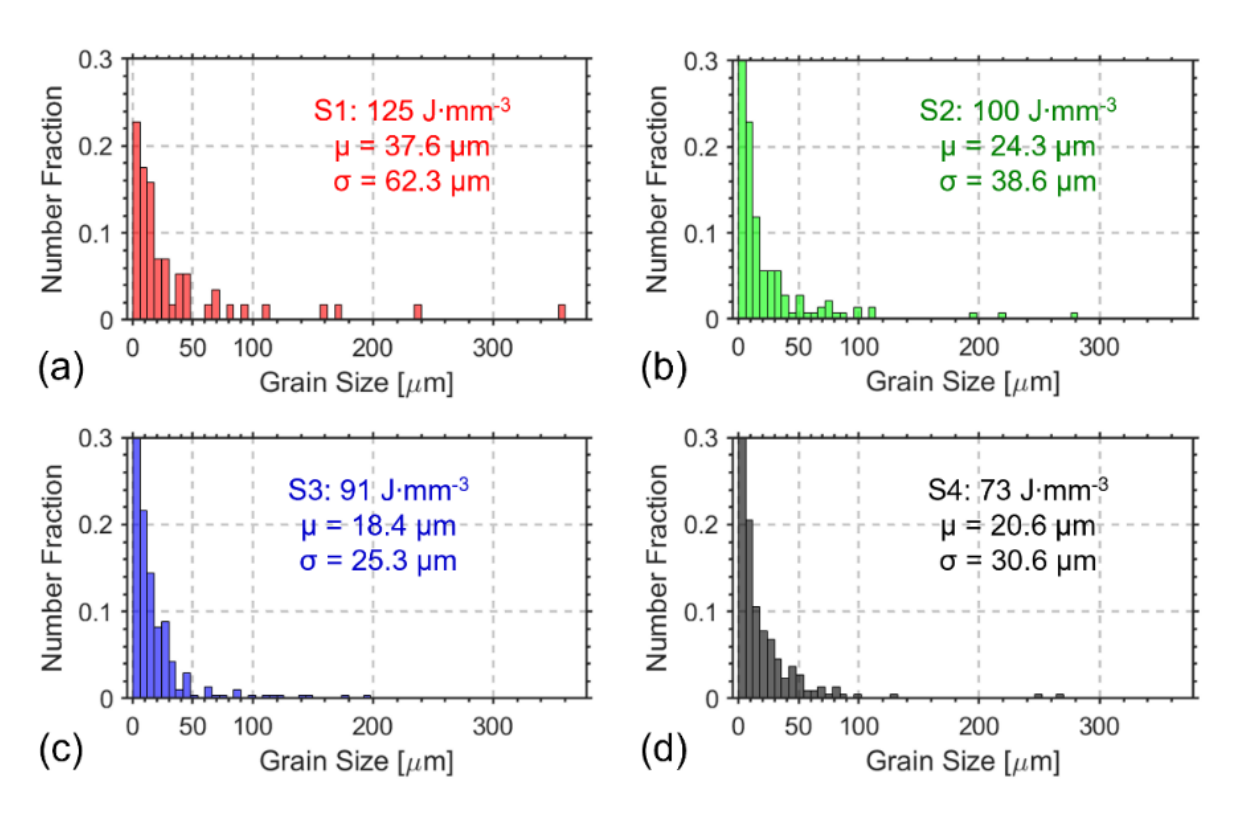


Figure 15. (a-d) Grain size distribution generated from the EBSD orientation maps for the treatment conditions S1-S4. High energy density in S1 leads to coarse columnar grains, and average grain size decreases from S1 to S2 with decreasing energy density. S3 has the lowest average grain size because of the low laser power used in this processing condition.

Correlation of Thermal History and Microstructure

In Figure 16, end-of-cycle temperature (T_e) and cooling rate (t_r) derived from the thermal simulations are correlated with experimentally measured grain size and primary dendritic arm spacing (PDAS). To explain further, in Figure 16, for each sample corresponding to the treatment condition S1-S4, the end-of-cycle temperature T_e from Figure 8(b) averaged over layer heights of 4 mm (layer 200) to 8 mm (layer 400) is plotted on the y-axis of Figure 16. Similarly, the cooling rate, t_r , averaged over layer height of 4 mm to 8 mm from Figure 8(a), are plotted on the x-axis.

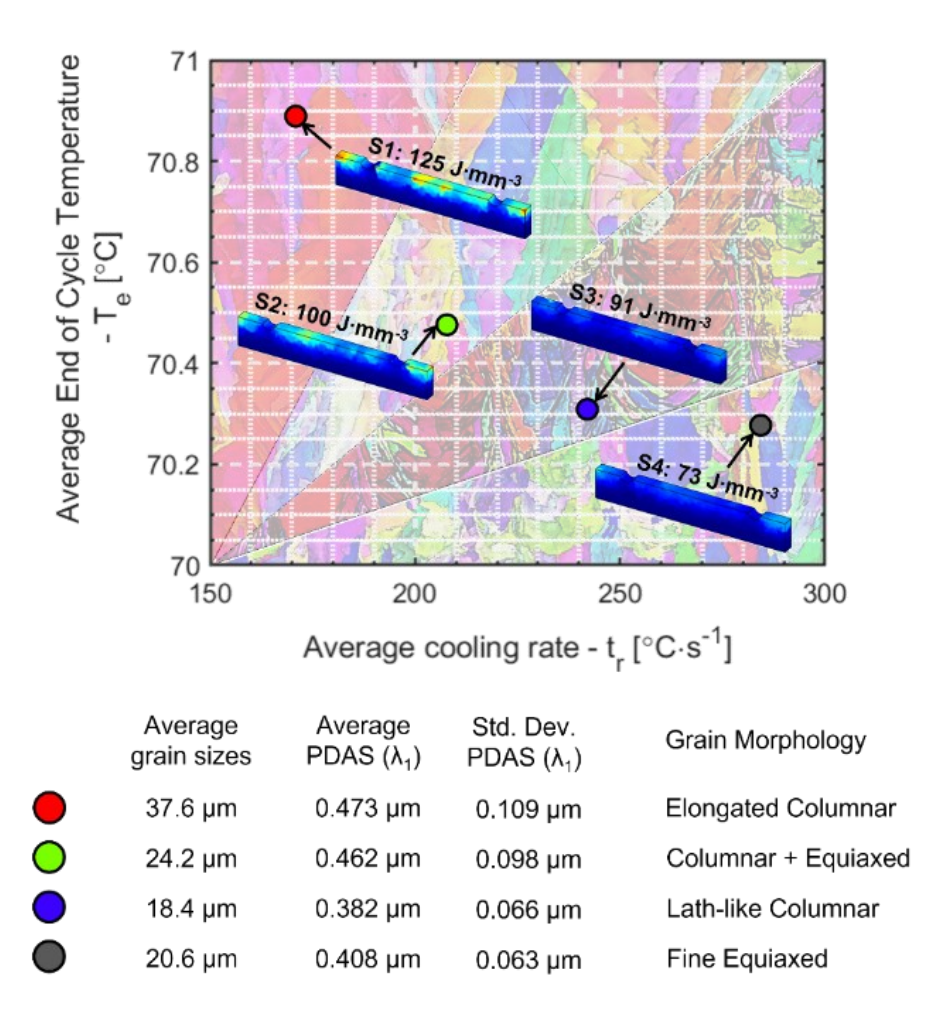


Figure 16. Correlation between end-of-cycle temperature (T_e) , cooling rates (t_r) , grain size and PDAS. End-of-cycle temperatures and cooling rates are averaged over layer heights of 4 to 8 mm. Average grain sizes are calculated from the EBSD maps and PDAS from SEM. Higher heat input lowers the cooling rate (t_r) and increases the end-of-cycle temperature (T_e) , results in epitaxial grain growth along the build direction and grains coarsen over multiple layers.

Subsequently, the grain size, dendritic arm spacing, and texture observed from EBSD are overlaid onto Figure 16. A lower t_r (i.e., low solidification velocity, R) and high T_e (i.e., high thermal gradient, G) are correlated to the coarser grains and wider dendritic arm spacing observed for S1 and S2. Similarly, high t_r and low T_e results in finer grains with a shorter dendritic spacing observed in S3 and S4 compared to S1 and S2; further, the higher t_r in S3 and S4 constrains grain growth within individual meltpools.

Figure 17 summarizes the results in the context of the process-thermal-structure-property relationship in the LPBF-processed SS316L samples. The following observations concerning treatment conditions S1, S3 and S4 are made relative to the nominal condition S2.

- For treatment condition S1 ($E_{\nu} \sim 125 \text{ J} \cdot \text{mm}^{-3}$), energy density was increased from the nominal processing condition S2 ($E_{\nu} \sim 100 \text{ J} \cdot \text{mm}^{-3}$) by increasing the laser power and decreasing the scan speed. Higher heat input in S1 relative to S2 enabled the columnar grains to coarsen, leading to epitaxial growth along the build direction across multiple layers.
- In S3 ($E_v \sim 91 \text{ J·mm}^{-3}$), the laser power and hatch spacing are reduced, which causes a lack-of-fusion porosity at the intersection of meltpool boundaries. A lower heat input leads to a finer microstructure. The short hatch spacing facilitates columnar grain growth, resulting in a lath-like structure. Epitaxial grain growth is observed along the build direction, originating at the center of the meltpool. Meanwhile, at the meltpool boundaries, the grains are observed to grow inwards towards the center of the meltpool. This peculiar growth pattern results in a mix of a fine microstructure along the meltpool boundaries with occasional coarse columnar grains along the center of the meltpool, akin to the solidified microstructure in ingot metal castings.

• The energy density for S4 ($E_v \sim 73 \text{ J} \cdot \text{mm}^{-3}$) is further decreased relative to S2 ($E_v = 100 \text{ J} \cdot \text{mm}^{-3}$) by reducing the laser power and increasing the scan speed. A lower heat input constrains the equiaxial grain growth within the individual meltpools and meltpool boundaries. In addition, a rapidly moving heat source also leads to a highly localized thermal gradient within the individual layer scans. It reduces the penetrative depth of the laser, leading to meltpool tearing under tensile loading, which is detrimental to the strength of LPBF parts.

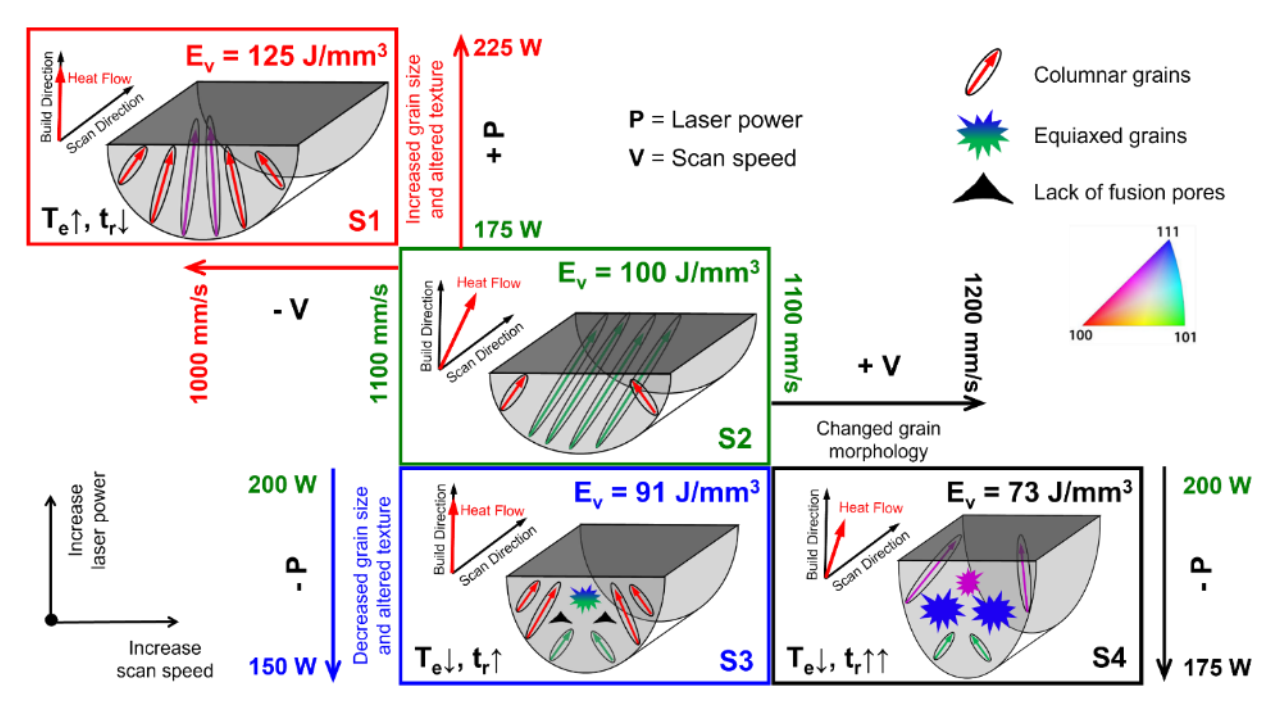


Figure 17. Summary of the process-thermal-structure relationship established from this study as a function of the processing parameters and the part's thermal history. The color and orientation of the arrows and equiaxed grains in the schematic represent the observed texture from EBSD measurements.

Mechanical Properties

3.6.1 Yield Strength and Ultimate Tensile Strength

Figure 18 (a) reports the tensile stress-strain curves obtained from digital image correlation 3.6 (DIC) tests of the four treatment conditions S1-S4. Three samples were tested per treatment condition, and the curves shown in Figure 18(a) represent one sample. Figure 18(b) illustrates the comparative bar graphs for the average yield strength (YS) and ultimate tensile strength (TS) for all four treatment conditions.

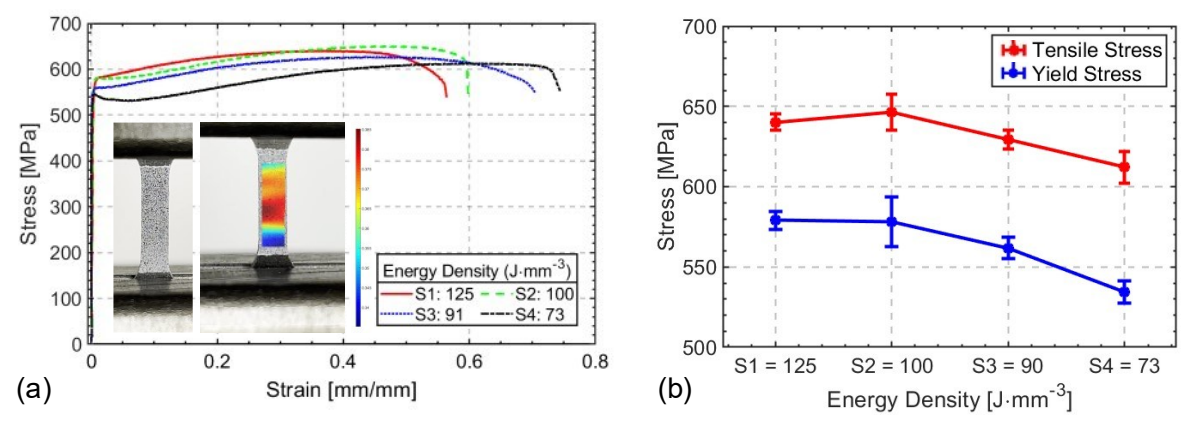


Figure 18. (a) Representative DIC tensile test results for conditions S1-S4. (b) Tensile stress and vield stress were ascertained from tensile curves (3 tests per set S1-S4).

Samples processed under treatment conditions S1 and S2 have comparable average YS with a difference of 0.2% (variation of 3.96%). The slightly higher strength in S2 compared with S1 can be explained by the Hall-Petch relationship. The cellular structure observed in LPBF parts shows the presence of dislocations at the cell boundaries. These dislocations transform the cellular structure into nano-sized grains [45]. The subsequent pinning of dislocations at these cell boundaries leads to work-hardening and improved YS and TS [77].

Despite their grain sizes being smaller, the YS and TS of S3 and S4 are significantly lesser than S1 and S2. This result is counter to the Hall-Petch relationship. The reduced strength of S3 is on account of lack-of-fusion porosity compared to S1 and S2. Further, although S3 is affected

by lack-of-fusion porosity, its strength is superior to S4. This is because the larger hatch spacing (H = 0.100 mm) in the case of S4 reduces the overlap between adjacent meltpools. The relatively weak bonding between adjacent tracks resulted in failure due to meltpool tearing. These phenomena are elucidated through fracture surface analysis in the forthcoming Sec 3.6.2.

Lastly, in Figure 18(a), the yielding behaviors are observed to be dependent on the processing conditions. While S1 depicts relatively continuous yielding, S4 exhibited discontinuous yielding behavior (decrease in stress after yielding). This phenomenon is explained because of the formation of Luder's bands observed in tensile testing of parts performed in-situ inside SEM. Representative results are reported in Appendix III.

3.6.2 Fracture Surface Analysis

Figure 19 shows the SEM images of the fracture surface of representative samples from all four treatment conditions. A high-resolution SEM fracture surface image displayed in Figure 19(a2) for sample S1 exhibits void coalescence artifacts termed dimples (green arrows). This artifact results from a dimple rupture propagating through the cellular structure [58]. Such an artifact is present in all samples, implying a highly ductile fracture mechanism consistent with the high strain observed in the tensile curves. It is expected that the size of the dimples is governed by the cell size (or the PDAS) and that dimple size decreases with a decrease in the grain size, which is consistent with the findings for conventionally manufactured SS316 [78].

Fracture surfaces of treatment conditions S1 & S3 have vertical step-like features (demarcated by red arrows in Figure 19(d1) and (d2)). These step-like features indicate a transgranular fracture mechanism; they are remnants of the tortuous crack path propagating through the local dendritic structure. These dendrites are oriented vertically inside the elongated columnar grains with a dominant <100> texture along the build direction in S1 and S3.

The fracture surface of S2 shown in Figure 19(b1) and (b2) is riddled with micro-cracks (demarcated by yellow arrows). As observed from EBSD in Figure 13(b), <101> is the dominant texture along the loading direction. In FCC materials, such as SS316L, <101> is the slip direction leading to more slip systems being activated in S2. Loading along the <101> direction also promotes twinning, which further aids the slip system activation [46, 79, 80]. These factors contribute to a higher strain hardening and plasticity in S2 than S1. The same behavior can be seen through the tortuous crack path leading to micro-cracks in S2.

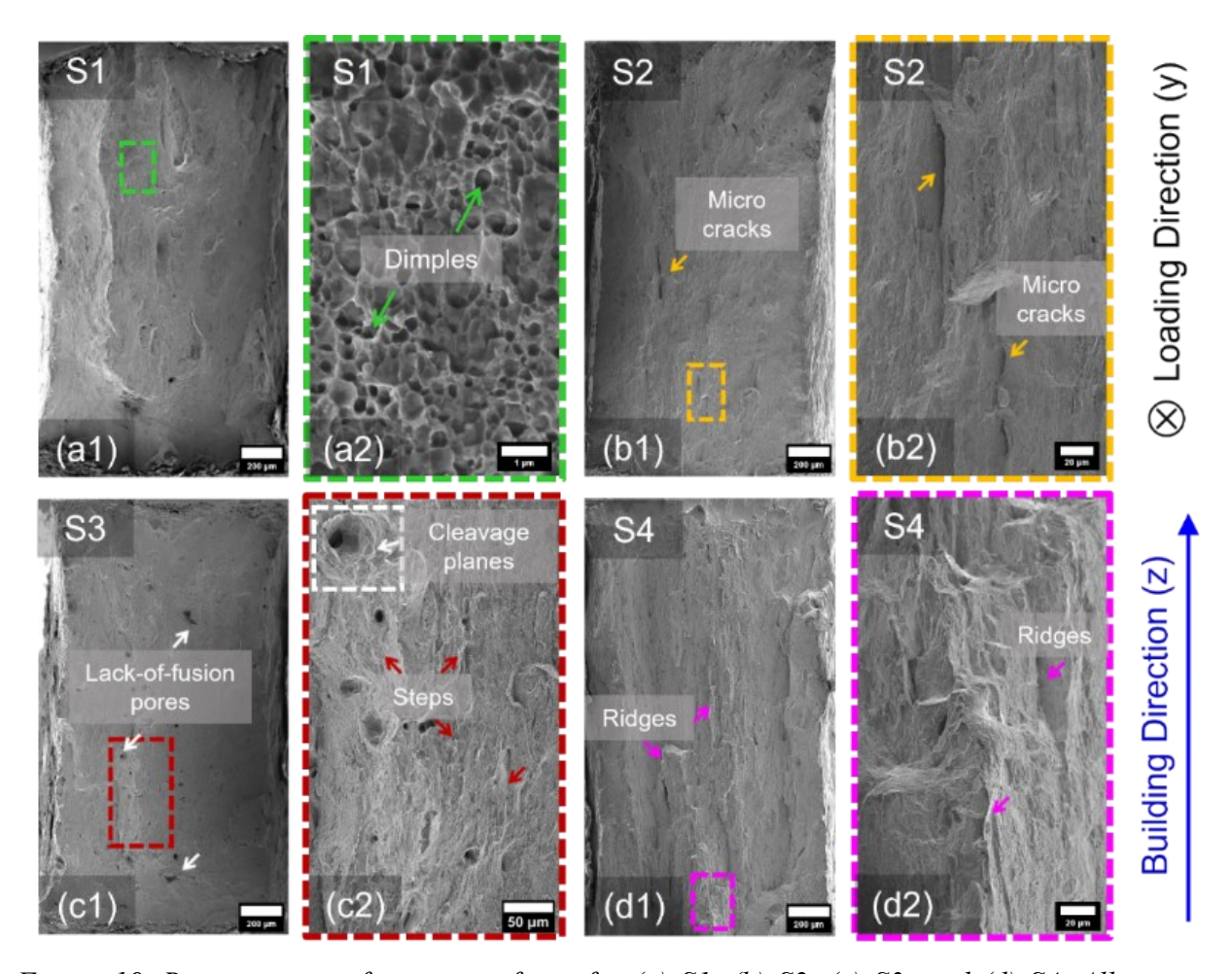


Figure 19. Representative fracture surfaces for (a) S1, (b) S2, (c) S3, and (d) S4. All coupons depict evidence of ductile dimple fracture. Additional features include micro-cracks in S2, local cleavage fracture around lack-of-fusion voids in S3, and layer-wise meltpool tearing in S4.

From Figure 19(c1) and (c2), the white arrows and white outline show the presence of lack-of-fusion voids in S3. A higher magnification image in Figure 19(d2) indicates the presence of cleavage planes hinting towards a local brittle fracture induced by these voids. Hence, even with the smallest grain size governing a better strength through the Hall-Petch relationship, a drop in strength is imminent for S3 compared to S1 and S2 due to lack-of-fusion porosity.

The fracture surface of S4 shown is shown in Figure 19(d1) and (d2). Deep ridges are visible on the fracture surface, highlighted by the pink arrows. These ridges show signs of the build layers tearing from one another, with the remnant damage visible on both halves of the tensile sample of condition S4. The lower energy density ($E_{\nu} \sim 73 \text{ J} \cdot \text{mm}^{-3}$) used for S4 does not promote grain growth across the meltpool boundaries (Figure 11(d1)), resulting in a weak interlayer adhesion, which in turn is associated with the meltpool tearing [40, 56]. The poor interlayer adhesion caused by insufficient meltpool penetration explains the lowest YS and TS observed in S4 (Figure 18).

3.6.3 Microhardness

Vickers microhardness values measured in the gauge section are reported in Figure 20 as a function of the four processing conditions. The microhardness trends correlate with the tensile and yield strength measurements reported in Figure 20. The hardness measurements for S1 and S2 are higher due to the lower impedance of the dislocation motion arising from a larger PDAS [81, 82]. The hardness measurements are reduced in S3 due to lack-of-fusion porosity. Treatment condition S4 has the lowest hardness due to the insufficient fusion of adjacent meltpools. This weaker interlayer adhesion also leads to meltpool tearing during DIC-tensile testing, as observed previously in Sec 3.6.1. Statistical analysis (ANOVA) affirms that the average microhardness measurements for S1-S4 are significantly different ($\alpha = 5\%$).

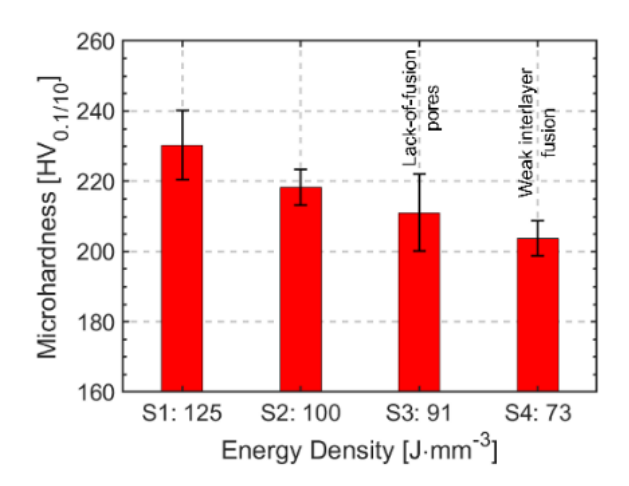


Figure 20. Microhardness measurement as a function of processing conditions S1-S4. Microhardness is proportional to energy density. S3 has a lower hardness value due to lack-offusion voids. S4 has the lowest hardness due to weak inter-layer bonding.

Conclusions and Future Work

4.

This work quantifies the causal effect of process parameters and thermal history on the microstructure and mechanical properties of stainless steel 316L parts made using the LPBF additive manufacturing process. Extensive empirical tests have been reported in the literature that link processing parameters to microstructure evolution and mechanical properties of stainless steel 316L [58]. However, the causal influence of thermal history aspects, such as cooling rate and interlayer temperature, on microstructure evolved and mechanical properties remain to be explained.

Since the thermal history is a function of process parameters, part shape, build layout, and material properties, not accounting for the effect of thermal history curtails existing understanding of process-structure-property relationships to specific cases geometries and build conditions. Consequently, practitioners are compelled to conduct expensive and time-consuming empirical studies, often requiring years, to optimize the processing parameters for every new part geometry [83]. This work addressed the foregoing gap by advancing an integrated experimental-computational framework to explain the causal effect of processing parameters on thermal history and, ultimately, the evolution of microstructure and part properties.

Specific outcomes from this work are as follows:

- 1. A total of 40 stainless steel 316L (SS316L) tensile test samples were produced under four treatment conditions of varying laser power, scan velocity, and hatch spacing. The samples were characterized using XCT (porosity), optical and scanning electron microscopy (meltpool and microstructure type), electron backscatter diffraction (grain size and orientation), and XRD (phases).
- 2. The thermal history of these samples was predicted using an experimentally validated mesh-free rapid thermal model. From the predicted thermal history, the cooling time (t_c) and end-of-cycle temperature (T_e) were quantified. The part-scale thermal history metrics (t_c and T_e) were related to the microstructure evolution in terms of the grain type, grain size distribution and microhardness. The higher the cooling rate (tr) and the smaller the end-of-cycle temperature (Te), the smaller the grain size. The processing conditions and thermal history were also related to lack-of-fusion porosity. A key finding in this regard is that the volumetric energy density (E_v) is not a good quantifier of flaw formation or microstructure evolution. The thermal history, in terms of the cooling rate and temperature gradients, is a more rigorous metric to correlate to microstructure and flaw formation.
- 3. The directionality, texture, and orientation of the microstructure have a significant effect on mechanical properties. These characteristics, in turn, are linked to the thermal history, specifically, t_r and T_e . A large T_e facilitates columnar, dendritic growth across multiple meltpools. Whereas the faster cooling rates and smaller thermal gradients are linked to fine cellular structures that are constricted within individual meltpools. Lastly, the thermal history also influences the failure mode via the microstructure evolved. Columnar grains were linked

to ductile fracture mode; shallow meltpools without overlapping grain growth are liable to result in meltpool tearing when subjected to tensile loads.

In our future work, we will endeavor to predict and control the microstructure and mechanical properties through multi-scale meltpool and part-level thermal history modeling.

References

- [1] A. Mostafaei, C. Zhao, Y. He, G.S. Reza, B. Shi, S. Shao, N. Shamsaei, Z. Wu, N. Kouraytem, T. Sun, J. Pauza, J.V. Gordon, B. Webler, N.D. Parab, M. Asherloo, Q. Guo, L. Chen, A.D. Rollett, *Defects and anomalies in powder bed fusion metal additive manufacturing*, Current Opinion in Solid State and Materials Science 26(2) (2022), 100974, doi: 10.1016/j.cossms.2021.100974.
- [2] M. Schmidt, M. Merklein, D. Bourell, D. Dimitrov, T. Hausotte, K. Wegener, L. Overmeyer, F. Vollertsen, G.N. Levy, *Laser based additive manufacturing in industry and academia*, CIRP Annals 66(2) (2017), 561-583, doi: 10.1016/j.cirp.2017.05.011.
- [3] I. Gibson, D. Rosen, B. Stucker, *Additive Manufacturing Technologies*, Springer, New York, 2015.
- [4] B. Blakey-Milner, P. Gradl, G. Snedden, M. Brooks, J. Pitot, E. Lopez, M. Leary, F. Berto, A. du Plessis, *Metal additive manufacturing in aerospace: A review*, Materials & Design 209 (2021), 110008, doi: 10.1016/j.matdes.2021.110008.
- [5] S. Mohd Yusuf, S. Cutler, N. Gao, *Review: The Impact of Metal Additive Manufacturing on the Aerospace Industry*, Metals 9(12) (2019), 1286, doi: 10.3390/met9121286.
- [6] Z. Snow, A.R. Nassar, E.W. Reutzel, *Invited Review Article: Review of the formation and impact of flaws in powder bed fusion additive manufacturing*, Additive Manufacturing 36 (2020), 101457, doi: 10.1016/j.addma.2020.101457.
- [7] E. Hosseini, V.A. Popovich, *A review of mechanical properties of additively manufactured Inconel 718*, Additive Manufacturing 30 (2019), 100877, doi: 10.1016/j.addma.2019.100877.
- [8] S. Ghorbanpour, K. Deshmukh, S. Sahu, T. Riemslag, E. Reinton, E. Borisov, A. Popovich, V. Bertolo, Q. Jiang, M.T. Sanchez, M. Knezevic, V. Popovich, *Additive manufacturing of functionally graded inconel 718: Effect of heat treatment and building orientation on microstructure and fatigue behaviour*, Journal of Materials Processing Technology 306 (2022), 117573, doi: 10.1016/j.jmatprotec.2022.117573.
- [9] A. Bandyopadhyay, K.D. Traxel, *Invited Review Article: Metal-additive manufacturing Modeling strategies for application-optimized designs*, Additive Manufacturing 22 (2018), 758-774, doi: 10.1016/j.addma.2018.06.024.
- [10] J.G. Michopoulos, A.P. Iliopoulos, J.C. Steuben, A.J. Birnbaum, S.G. Lambrakos, *On the multiphysics modeling challenges for metal additive manufacturing processes*, Additive Manufacturing 22 (2018), 784-799, doi: 10.1016/j.addma.2018.06.019.
- [11] W.J. Sames, F.A. List, S. Pannala, R.R. Dehoff, S.S. Babu, *The metallurgy and processing science of metal additive manufacturing*, International Materials Reviews 61(5) (2016), 315-360, doi: 10.1080/09506608.2015.1116649.
- [12] T.G. Spears, S.A. Gold, *In-process sensing in selective laser melting (SLM) additive manufacturing*, Integrating Materials and Manufacturing Innovation 5(1) (2016), 16-40, doi: 10.1186/s40192-016-0045-4.
- [13] P. Foteinopoulos, A. Papacharalampopoulos, P. Stavropoulos, *On thermal modeling of Additive Manufacturing processes*, CIRP Journal of Manufacturing Science and Technology 20 (2018), 66-83, doi: 10.1016/j.cirpj.2017.09.007.

- [14] R.J. Williams, A. Piglione, T. Rønneberg, C. Jones, M.-S. Pham, C.M. Davies, P.A. Hooper, In situ thermography for laser powder bed fusion: Effects of layer temperature on porosity, microstructure and mechanical properties, Additive Manufacturing 30 (2019), 100880, doi: 10.1016/j.addma.2019.100880.
- [15] S. Sanchez, P. Smith, Z. Xu, G. Gaspard, C.J. Hyde, W.W. Wits, I.A. Ashcroft, H. Chen, A.T. Clare, *Powder Bed Fusion of nickel-based superalloys: A review*, International Journal of Machine Tools and Manufacture 165 (2021), 103729, doi: 10.1016/j.ijmachtools.2021.103729.
- [16] A. Mostafaei, R. Ghiaasiaan, I.T. Ho, S. Strayer, K.-C. Chang, N. Shamsaei, S. Shao, S. Paul, A.-C. Yeh, S. Tin, A.C. To, *Additive Manufacturing of Nickel-based superalloys: a state-of-the-art review on process-structure-defect-property relationship*, Progress in Materials Science (2023), 101108, doi: 10.1016/j.pmatsci.2023.101108.
- [17] G. Mohr, S.J. Altenburg, K. Hilgenberg, On the limitations of small cubes as test coupons for process parameter optimization in laser powder bed fusion of metals, Journal of Laser Applications 35(4) (2023), 042029, doi: 10.2351/7.0001080.
- [18] R. Yavari, Z. Smoqi, A. Riensche, B. Bevans, H. Kobir, H. Mendoza, H. Song, K. Cole, P. Rao, *Part-scale thermal simulation of laser powder bed fusion using graph theory: Effect of thermal history on porosity, microstructure evolution, and recoater crash*, Materials & Design 204 (2021), 109685, doi: 10.1016/j.matdes.2021.109685.
- [19] Z. Liu, D. Zhao, P. Wang, M. Yan, C. Yang, Z. Chen, J. Lu, Z. Lu, *Additive manufacturing of metals: Microstructure evolution and multistage control*, Journal of Materials Science & Technology 100 (2022), 224-236, doi: 10.1016/j.jmst.2021.06.011.
- [20] S.A. Khairallah, A.T. Anderson, A. Rubenchik, W.E. King, Laser powder-bed fusion additive manufacturing: Physics of complex melt flow and formation mechanisms of pores, spatter, and denudation zones, Acta Materialia 108 (2016), 36-45, doi: 10.1016/j.actamat.2016.02.014.
- [21] W. King, A. Anderson, R. Ferencz, N. Hodge, C. Kamath, S. Khairallah, *Overview of modelling and simulation of metal powder-bed fusion process at Lawrence Livermore National Laboratory*, Materials Science and Technology 31(8) (2014), 957-968, doi:
- [22] J.V. Gordon, S.P. Narra, R.W. Cunningham, H. Liu, H. Chen, R.M. Suter, J.L. Beuth, A.D. Rollett, *Defect structure process maps for laser powder bed fusion additive manufacturing*, Additive Manufacturing 36 (2020), 101552, doi: 10.1016/j.addma.2020.101552.
- [23] G.L. Knapp, B. Stump, L. Scime, A. Márquez Rossy, C. Joslin, W. Halsey, A. Plotkowski, Leveraging the digital thread for physics-based prediction of microstructure heterogeneity in additively manufactured parts, Additive Manufacturing 78 (2023), 103861, doi: 10.1016/j.addma.2023.103861.
- [24] A. Gaikwad, R.J. Williams, H. de Winton, B.D. Bevans, Z. Smoqi, P. Rao, P.A. Hooper, *Multi phenomena melt pool sensor data fusion for enhanced process monitoring of laser powder bed fusion additive manufacturing*, Materials & Design 221 (2022), 110919, doi: 10.1016/j.matdes.2022.110919.
- [25] Z. Smoqi, A. Gaikwad, B. Bevans, M.H. Kobir, J. Craig, A. Abul-Haj, A. Peralta, P. Rao, *Monitoring and prediction of porosity in laser powder bed fusion using physics-informed meltpool signatures and machine learning*, Journal of Materials Processing Technology 304 (2022), 117550, doi: 10.1016/j.jmatprotec.2022.117550.

- [26] C. Schwerz, L. Nyborg, Linking In Situ Melt Pool Monitoring to Melt Pool Size Distributions and Internal Flaws in Laser Powder Bed Fusion, Metals 11(11) (2021), 1856, doi: 10.3390/met11111856.
- [27] A.R. Nassar, M.A. Gundermann, E.W. Reutzel, P. Guerrier, M.H. Krane, M.J. Weldon, Formation processes for large ejecta and interactions with melt pool formation in powder bed fusion additive manufacturing, Sci Rep 9(1) (2019), 5038, doi: 10.1038/s41598-019-41415-7.
- [28] Z. Wu, G. Tang, S.J. Clark, A. Meshkov, S. Roychowdhury, B. Gould, V. Ostroverkhov, T. Adcock, S.J. Duclos, K. Fezzaa, C. Immer, A.D. Rollett, *High frequency beam oscillation keyhole dynamics in laser melting revealed by in-situ x-ray imaging*, Communications Materials 4(1) (2023), 5, doi: 10.1038/s43246-023-00332-z.
- [29] S. Chowdhury, N. Yadaiah, C. Prakash, S. Ramakrishna, S. Dixit, L.R. Gupta, D. Buddhi, Laser powder bed fusion: a state-of-the-art review of the technology, materials, properties & defects, and numerical modelling, Journal of Materials Research and Technology 20 (2022), 2109-2172, doi: 10.1016/j.jmrt.2022.07.121.
- [30] S.R. Narasimharaju, W. Zeng, T.L. See, Z. Zhu, P. Scott, X. Jiang, S. Lou, *A comprehensive review on laser powder bed fusion of steels: Processing, microstructure, defects and control methods, mechanical properties, current challenges and future trends*, Journal of Manufacturing Processes 75 (2022), 375-414, doi: 10.1016/j.jmapro.2021.12.033.
- [31] J. Zhou, X. Han, H. Li, S. Liu, J. Yi, *Investigation of layer-by-layer laser remelting to improve surface quality, microstructure, and mechanical properties of laser powder bed fused AlSi10Mg alloy*, Materials & Design 210 (2021), 110092, doi: 10.1016/j.matdes.2021.110092.
- [32] N. Ahmed, I. Barsoum, G. Haidemenopoulos, R.K.A. Al-Rub, *Process parameter selection and optimization of laser powder bed fusion for 316L stainless steel: A review*, Journal of Manufacturing Processes 75 (2022), 415-434, doi: 10.1016/j.jmapro.2021.12.064.
- [33] A. Riensche, B.D. Bevans, Z. Smoqi, R. Yavari, A. Krishnan, J. Gilligan, N. Piercy, K. Cole, P. Rao, *Feedforward control of thermal history in laser powder bed fusion: Toward physics-based optimization of processing parameters*, Materials & Design 224 (2022), 111351, doi: 10.1016/j.matdes.2022.111351.
- [34] J. Munk, E. Breitbarth, T. Siemer, N. Pirch, C. Häfner, *Geometry Effect on Microstructure and Mechanical Properties in Laser Powder Bed Fusion of Ti-6Al-4V*, Metals 12(3) (2022), 482, doi: 10.3390/met12030482.
- [35] V. Chahal, R.M. Taylor, *A review of geometric sensitivities in laser metal 3D printing*, Virtual and Physical Prototyping 15(2) (2020), 227-241, doi: 10.1080/17452759.2019.1709255.
- [36] L. Ladani, M. Sadeghilaridjani, *Review of Powder Bed Fusion Additive Manufacturing for Metals*, Metals 11(9) (2021), 1391, doi: 10.3390/met11091391.
- [37] P. Bajaj, A. Hariharan, A. Kini, P. Kürnsteiner, D. Raabe, E.A. Jägle, *Steels in additive manufacturing: A review of their microstructure and properties*, Materials Science and Engineering: A 772 (2020), 138633, doi: 10.1016/j.msea.2019.138633.
- [38] N. Haghdadi, M. Laleh, M. Moyle, S. Primig, *Additive manufacturing of steels: a review of achievements and challenges*, Journal of Materials Science 56(1) (2021), 64-107, doi: 10.1007/s10853-020-05109-0.

- [39] K. Sommer, L. Agudo Jácome, R. Hesse, D. Bettge, *Revealing the Nature of Melt Pool Boundaries in Additively Manufactured Stainless Steel by Nano-Sized Modulation*, Advanced Engineering Materials 24(6) (2022), 2101699, doi: 10.1002/adem.202101699.
- [40] W. Shifeng, L. Shuai, W. Qingsong, C. Yan, Z. Sheng, S. Yusheng, *Effect of molten pool boundaries on the mechanical properties of selective laser melting parts*, Journal of Materials Processing Technology 214(11) (2014), 2660-2667, doi: 10.1016/j.jmatprotec.2014.06.002.
- [41] R.W. Fonda, D.J. Rowenhorst, *Crystallographic Variability in Additive Manufacturing*, 42nd Risø International Symposium on Materials Science 1249 (2022), 012007, doi: 10.1088/1757-899X/1249/1/012007.
- [42] T. Niendorf, S. Leuders, A. Riemer, H.A. Richard, T. Tröster, D. Schwarze, *Highly Anisotropic Steel Processed by Selective Laser Melting*, Metallurgical and Materials Transactions B 44(4) (2013), 794-796, doi: 10.1007/s11663-013-9875-z.
- [43] H.L. Wei, J. Mazumder, T. DebRoy, Evolution of solidification texture during additive manufacturing, Sci Rep 5 (2015), 16446, doi: 10.1038/srep16446.
- [44] A. Basak, S. Das, *Epitaxy and Microstructure Evolution in Metal Additive Manufacturing*, Annual Review of Materials Research 46(1) (2016), 125-149, doi: 10.1146/annurev-matsci-070115-031728.
- [45] K.M. Bertsch, G. Meric de Bellefon, B. Kuehl, D.J. Thoma, *Origin of dislocation structures in an additively manufactured austenitic stainless steel 316L*, Acta Materialia 199 (2020), 19-33, doi: 10.1016/j.actamat.2020.07.063.
- [46] S. Tekumalla, B. Selvarajou, S. Raman, S. Gao, M. Seita, *The role of the solidification structure on orientation-dependent hardness in stainless steel 316L produced by laser powder bed fusion*, Materials Science and Engineering: A 833 (2022), 142493, doi: 10.1016/j.msea.2021.142493.
- [47] S. Ghorbanpour, S. Sahu, K. Deshmukh, E. Borisov, T. Riemslag, E. Reinton, V. Bertolo, Q. Jiang, A. Popovich, A. Shamshurin, M. Knezevic, V. Popovich, *Effect of microstructure induced anisotropy on fatigue behaviour of functionally graded Inconel 718 fabricated by additive manufacturing*, Materials Characterization 179 (2021), 111350, doi: 10.1016/j.matchar.2021.111350.
- [48] A.K. Agrawal, B. Rankouhi, D.J. Thoma, *Predictive process mapping for laser powder bed fusion: A review of existing analytical solutions*, Current Opinion in Solid State & Materials Science 26 (2022), 101024, doi: 10.1016/j.cossms.2022.101024.
- [49] A.K. Agrawal, G. Meric de Bellefon, D. Thoma, *High-throughput experimentation for microstructural design in additively manufactured 316L stainless steel*, Materials Science and Engineering: A 793 (2020), 139841, doi: 10.1016/j.msea.2020.139841.
- [50] M. Gor, H. Soni, V. Wankhede, P. Sahlot, K. Grzelak, I. Szachgluchowicz, J. Kluczyński, A Critical Review on Effect of Process Parameters on Mechanical and Microstructural Properties of Powder-Bed Fusion Additive Manufacturing of SS316L, Materials 14(21) (2021), 6527, doi: 10.3390/ma14216527.

- [51] N. Diaz Vallejo, C. Lucas, N. Ayers, K. Graydon, H. Hyer, Y. Sohn, *Process Optimization and Microstructure Analysis to Understand Laser Powder Bed Fusion of 316L Stainless Steel*, Metals 11(5) (2021), 832, doi: 10.3390/met11050832.
- [52] B. Zhou, P. Xu, W. Li, Y. Liang, Y. Liang, Microstructure and Anisotropy of the Mechanical Properties of 316L Stainless Steel Fabricated by Selective Laser Melting, Metals 11(5) (2021), 775, doi: 10.3390/met11050775.
- [53] J. Suryawanshi, K.G. Prashanth, U. Ramamurty, *Mechanical behavior of selective laser melted 316L stainless steel*, Materials Science and Engineering: A 696 (2017), 113-121, doi: 10.1016/j.msea.2017.04.058.
- [54] D. Wang, C. Song, Y. Yang, Y. Bai, *Investigation of crystal growth mechanism during selective laser melting and mechanical property characterization of 316L stainless steel parts*, Materials & Design 100 (2016), 291-299, doi: 10.1016/j.matdes.2016.03.111.
- [55] D. Yang, Y. Yin, X. Kan, Y. Zhao, Z. Zhao, J. Sun, *The mechanism of substructure formation and grain growth 316L stainless steel by selective laser melting*, Materials Research Express 8(9) (2021), doi: 10.1088/2053-1591/ac21ea.
- [56] J. Liu, Y. Song, C. Chen, X. Wang, H. Li, C.a. Zhou, J. Wang, K. Guo, J. Sun, *Effect of scanning speed on the microstructure and mechanical behavior of 316L stainless steel fabricated by selective laser melting*, Materials & Design 186 (2020), 108355, doi: 10.1016/j.matdes.2019.108355.
- [57] Q. Liu, G. Wang, C. Qiu, On the role of dynamic grain movement in deformation and mechanical anisotropy development in a selectively laser melted stainless steel, Additive Manufacturing 35 (2020), 101329, doi: 10.1016/j.addma.2020.101329.
- [58] A. Leicht, M. Rashidi, U. Klement, E. Hryha, *Effect of process parameters on the microstructure, tensile strength and productivity of 316L parts produced by laser powder bed fusion*, Materials Characterization 159 (2020), 110016, doi: 10.1016/j.matchar.2019.110016.
- [59] Y.n. Song, Q. Sun, K. Guo, X. Wang, J. Liu, J. Sun, Effect of scanning strategies on the microstructure and mechanical behavior of 316L stainless steel fabricated by selective laser melting, Materials Science and Engineering: A 793 (2020), 139879, doi: 10.1016/j.msea.2020.139879.
- [60] A. Leicht, U. Klement, E. Hryha, *Effect of build geometry on the microstructural development of 316L parts produced by additive manufacturing*, Materials Characterization 143 (2018), 137-143, doi: 10.1016/j.matchar.2018.04.040.
- [61] M.R. Yavari, K.D. Cole, P. Rao, *Thermal Modeling in Metal Additive Manufacturing Using Graph Theory*, Journal of Manufacturing Science and Engineering 141(7) (2019), 071007, doi: 10.1115/1.4043648.
- [62] R. Yavari, R. Williams, A. Riensche, P.A. Hooper, K.D. Cole, L. Jacquemetton, H. Halliday, P.K. Rao, *Thermal modeling in metal additive manufacturing using graph theory Application to laser powder bed fusion of a large volume impeller*, Additive Manufacturing 41 (2021), 101956, doi: 10.1016/j.addma.2021.101956.

- [63] D. Yang, Y. Yin, X. Kan, Y. Zhao, Z. Zhao, J. Sun, *The mechanism of substructure formation and grain growth 316L stainless steel by selective laser melting*, Materials Research Express 8(9) (2021), 096510, doi: 10.1088/2053-1591/ac21.
- [64] A. Gaikwad, B. Giera, G.M. Guss, J.-B. Forien, M.J. Matthews, P. Rao, *Heterogeneous sensing and scientific machine learning for quality assurance in laser powder bed fusion A single-track study*, Additive Manufacturing 36 (2020), 101659, doi: 10.1016/j.addma.2020.101659.
- [65] ISO/ASTM Standard 52900; 'Additive manufacturing General principles Fundamentals and vocabulary', 2021, url: https://www.astm.org/f3177-21.html.
- [66] J.P. Oliveira, T.G. Santos, R.M. Miranda, Revisiting fundamental welding concepts to improve additive manufacturing: From theory to practice, Progress in Materials Science 107 (2020), 100590, doi: 10.1016/j.pmatsci.2019.100590.
- [67] M. Gouge, P. Michaleris, E. Denlinger, J. Irwin, *The Finite Element Method for the Thermo-Mechanical Modeling of Additive Manufacturing Processes*, Thermo-Mechanical Modeling of Additive Manufacturing, First Edition, Elsevier, 2018.
- [68] B. Schoinochoritis, D. Chantzis, K. Salonitis, *Simulation of metallic powder bed additive manufacturing processes with the finite element method: A critical review*, Proceedings of the Institution of Mechanical Engineers, Part B: Journal of Engineering Manufacture 231(1) (2016), 96-117, doi: 10.1177/0954405414567522.
- [69] Z. Luo, Y. Zhao, A survey of finite element analysis of temperature and thermal stress fields in powder bed fusion Additive Manufacturing, Additive Manufacturing 21 (2018), 318-332, doi: 10.1016/j.addma.2018.03.022.
- [70] J. Baiges, M. Chiumenti, C.A. Moreira, M. Cervera, R. Codina, *An adaptive Finite Element strategy for the numerical simulation of additive manufacturing processes*, Additive Manufacturing 37 (2021), doi: 10.1016/j.addma.2020.101650.
- [71] A.R. Riensche, B.D. Bevans, G. King, A. Krishnan, K.D. Cole, P. Rao, *Predicting meltpool depth and primary dendritic arm spacing in laser powder bed fusion additive manufacturing using physics-based machine learning*, Materials & Design 237 (2024), 112540, doi: 10.1016/j.matdes.2023.112540.
- [72] J. Ye, S.A. Khairallah, A.M. Rubenchik, M.F. Crumb, G. Guss, J. Belak, M.J. Matthews, *Energy Coupling Mechanisms and Scaling Behavior Associated with Laser Powder Bed Fusion Additive Manufacturing*, Advanced Engineering Materials 21(7) (2019), doi: 10.1002/adem.201900185.
- [73] R. Yavari, A. Riensche, E. Tekerek, L. Jacquemetton, H. Halliday, M. Vandever, A. Tenequer, V. Perumal, A. Kontsos, Z. Smoqi, K. Cole, P. Rao, *Digitally twinned additive manufacturing: Detecting flaws in laser powder bed fusion by combining thermal simulations with in-situ meltpool sensor data*, Materials & Design 211 (2021), 110167, doi: 10.1016/j.matdes.2021.110167.
- [74] T. DebRoy, H.L. Wei, J.S. Zuback, T. Mukherjee, J.W. Elmer, J.O. Milewski, A.M. Beese, A. Wilson-Heid, A. De, W. Zhang, *Additive manufacturing of metallic components Process, structure and properties*, Progress in Materials Science 92 (2018), 112-224, doi: 10.1016/j.pmatsci.2017.10.001.

- [75] H. Schönmaier, R. Krein, M. Schmitz-Niederau, R. Schnitzer, *Influence of the Heat Input on the Dendritic Solidification Structure and the Mechanical Properties of 2.25Cr-1Mo-0.25V Submerged-Arc Weld Metal*, Journal of Materials Engineering and Performance 30(10) (2021), 7138-7151, doi: 10.1007/s11665-021-05922-x.
- [76] S. Gao, Z. Hu, M. Duchamp, P.S.S.R. Krishnan, S. Tekumalla, X. Song, M. Seita, *Recrystallization-based grain boundary engineering of 316L stainless steel produced via selective laser melting*, Acta Materialia 200 (2020), 366-377, doi: 10.1016/j.actamat.2020.09.015.
- [77] S.-H. Li, Y. Zhao, P. Kumar, U. Ramamurty, Effect of initial dislocation density on the plastic deformation response of 316L stainless steel manufactured by directed energy deposition, Materials Science and Engineering: A 851 (2022), doi: 10.1016/j.msea.2022.143591.
- [78] W. Qin, J. Li, Y. Liu, J. Kang, L. Zhu, D. Shu, P. Peng, D. She, D. Meng, Y. Li, *Effects of grain size on tensile property and fracture morphology of 316L stainless steel*, Materials Letters 254 (2019), 116-119, doi: 10.1016/j.matlet.2019.07.058.
- [79] X. Wang, B. Zheng, K. Yu, S. Jiang, E.J. Lavernia, J.M. Schoenung, *The role of cell boundary orientation on mechanical behavior: A site-specific micro-pillar characterization study*, Additive Manufacturing 46 (2021), 102154, doi: 10.1016/j.addma.2021.102154.
- [80] X. Yang, X. Wang, M. Brochu, X. Wang, N.M. Harrison, S.B. Leen, J. Segurado, *Understanding orientation-dependent plasticity in laser beam powder bed fusion stainless steel through crystal plasticity modelling*, Materials Science and Engineering: A 852 (2022), 143682, doi: 10.1016/j.msea.2022.143682.
- [81] S. Kurian, R. Mirzaeifar, *Deformation mechanisms of the subgranular cellular structures in selective laser melted 316L stainless steel*, Mechanics of Materials 148 (2020), 103478, doi: 10.1016/j.mechmat.2020.103478.
- [82] Y. Zhong, Sub-grain structure in additive manufactured stainless steel 316L, PhD dissertation, Department of Materials and Environmental Chemistry, Stockholm University, 2017.
- [83] M. Seifi, M. Gorelik, J. Waller, N. Hrabe, N. Shamsaei, S. Daniewicz, J.J. Lewandowski, *Progress Towards Metal Additive Manufacturing Standardization to Support Qualification and Certification*, Jom 69(3) (2017), 439-455, doi: 10.1007/s11837-017-2265-2.
- [84] M.N. Gussev, D.A. McClintock, T.G. Lach, *Origin, parameters, and underlying deformation mechanisms of propagating deformation bands in irradiated 316L stainless steel*, Acta Materialia 242 (2023), 118434, doi: 10.1016/j.actamat.2022.118434.

Appendix I - Thermal Model Calibration and Validation

A 42 mm tall bell crank geometry, shown in Figure 21(a), was printed to calibrate the boundary conditions and heat loss coefficients and, subsequently, validate the graph theory predictions. This geometry was manufactured using the nominal processing condition S2 on the same EOS M290 LPBF machine and with identical SS316L powder material used in this work. Once calibrated, the same model parameters were used to predict the thermal history of the tensile test samples proposed in this work (Figure 4).

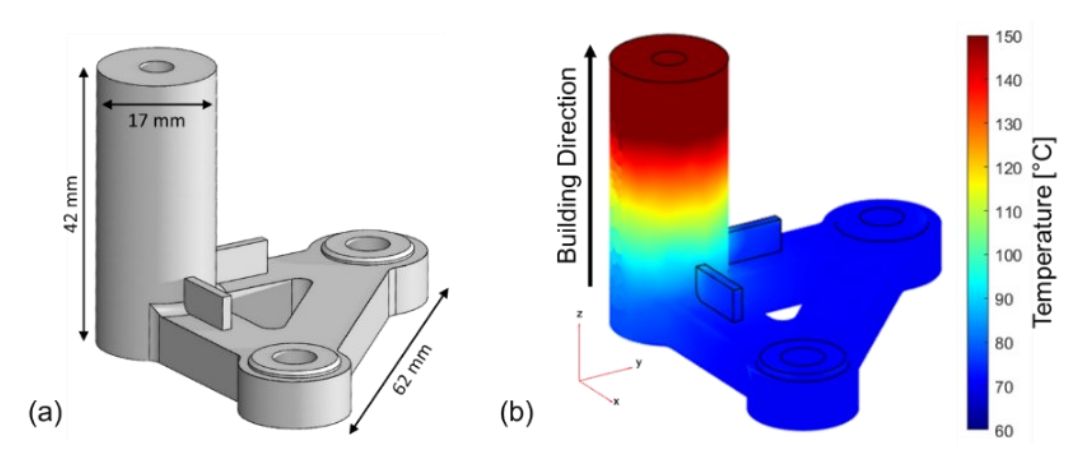


Figure 21. (a) A CAD drawing of the bell-crank geometry was used to identify the heat losses and calibrate the graph theory thermal model. The same EOS M290 machine makes this geometry with SS316L material used in this study. (b) Average end-of-cycle layer temperature distribution of the bell-crank geometry simulated from the calibrated graph theory model.

A brief procedure for the model calibration is summarized herewith. Details are available in our prior publications [18, 33]. Part surface temperature readings were obtained from a longwave infrared (LWIR) thermal camera installed inside the LPBF machine. The LWIR camera was calibrated to an absolute temperature scale using an industry-standard contact thermocouple-based approach described in our previous works [18, 33]. This infrared thermal camera measures the average end-of-cycle layer temperature, which is the mean temperature of an entire layer after a new layer is deposited on top, just before the melting of the new layer is initiated by the laser. As shown in Figure 22, the average end-of-cycle layer temperature for the bell crank predicted

from the graph theory thermal model agrees closely with the observed infrared thermal camera measurements. The root mean squared error (RMSE) and symmetric mean average percentage (SMAPE) are within 6 °C and 3 %, respectively, and the graph theory model converged within 30 minutes for this complex part.

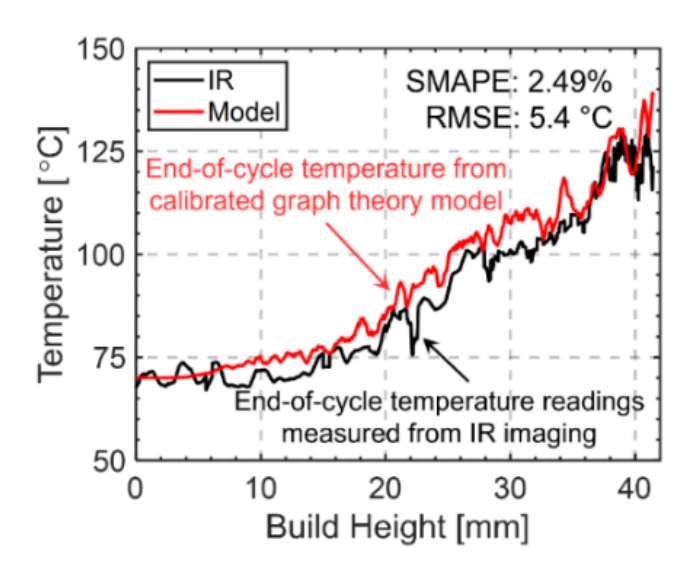


Figure 22. Calibration results show the predicted end-of-cycle temperatures compared against the real-time IR imaging as the ground truth.

Appendix II - X-ray diffraction

Phases formed in the SS316L samples were identified by XRD (Bruker XRD D8) using 0.1540 nm wavelength Cu Kα radiation between 40 to 80° with a step size of 0.02 °·s⁻¹ and exposure time of 1 s·step⁻¹. From the XRD peaks reported in Figure 23, the presence of a single phase γ-austenite is inferred for all treatment conditions S1-S4. The presence of a single austenitic phase is consistent with the observations from previous works on LPBF of SS316L [56, 63, 76]. This is an important observation because the effect of part-level thermal history on secondary phases is not warranted in this work. The presence of a single austenitic phase means that the grain size and primary dendritic arm spacing are the key microstructure features affected; consequently, these are the two central microstructure-related aspects studied herein.

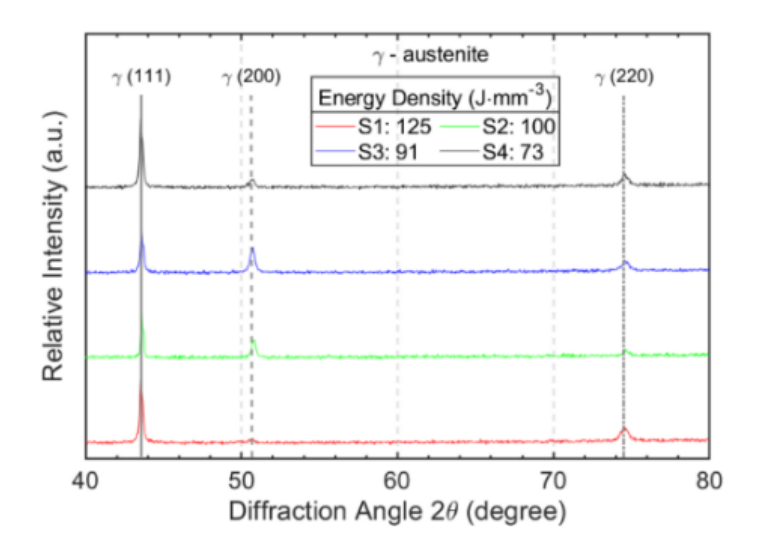


Figure 23. X-ray diffraction curves of SS316L printed by LPBF with varying energy densities from S1-S4. 316L SS forms a single-phase γ -austenite in all the sets used in this study.

Appendix III – In-situ SEM tensile testing

In Figure 24(a), the tensile curves of processing condition S4 exhibit a discontinuous yielding behavior compared to the other processing conditions. To explain this phenomenon, tensile experiments were performed in situ in an SEM. Figure 24(b) shows an SEM image of one such tensile test that was stopped in situ after the yielding point was reached. The discontinuous yielding is attributed to the formation of striations similar to Luder's bands at the yielding point, which leads to prolonged yielding and a drop in the flow stress post-yielding [84]. The formation of Luder's band in SS316L is highly dependent on orientation and grain size, which explains why it is present only in sample S4.

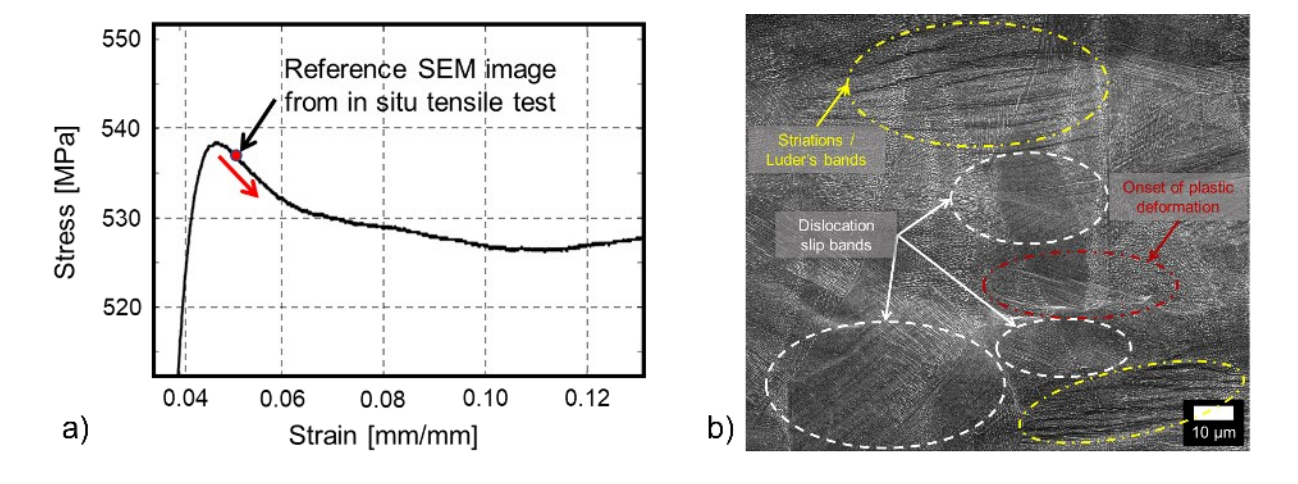


Figure 24. (a) Tensile curve from the in situ tensile test, (b) SEM image from the in situ tensile tests performed on a tensile sample from processing condition S4 and stopped at a strain value of 0.05. The tensile test is stopped after the yielding point is reached and the flow stress starts decreasing. In addition to the local dislocation slip bands, S4 also exhibits striations (much like Luder's bands) that span across multiple meltpools.

Acknowledgments

Kaustubh Deshmukh, Ryan J. Lane, Reza Mirzaeifar (deceased), Christopher B. Williams, and Prahalada Rao acknowledge funding for this research through the Department of the Navy award number N00014-21-1-2781 issued by the Office of Naval Research.

Harold (Scott) Halliday thanks the NSF for funding the work carried out at Navajo Technical University through HRD 1840138 (NTU Center for Advanced Manufacturing).

Prahalada Rao acknowledges funding from the National Science Foundation (NSF) via Grant numbers: CMMI-2309483/1752069, OIA-1929172, PFI-TT 2322322/2044710, CMMI-1920245, ECCS-2020246, CMMI-1739696, and CMMI-1719388 for funding his research program, and the National Institute of Standards and Technology (NIST) via grant 70NANB23H029T for supporting his research program.

- Understanding the causal influence of process parameters and thermal history on part quality and detection of defect formation using in-situ sensing was the major aspect of CMMI-2309483/1752069 (Program Officer: Andy Wells). This grant partially funded the graduate work of Alex Riensche and Ben Bevans.
- Commercialization of the graph theory thermal approach for ultrafast simulation of metal additive manufacturing processes is being pursued under PFI-TT 2322322/2044710 (Program Officer: Samir Iqbal). This grant partially funded the graduate work of Alex Riensche and Ben Bevans.
- Predicting (detecting) flaws in laser powder bed fusion by combining thermal simulations with in-situ sensor data was funded via NIST 70NANB23H029T.

The samples used in this work were fabricated at Commonwealth Center for Advanced Manufacturing through the assistance of Kyle Snyder.

This work used shared facilities at the Nanoscale Characterization and Fabrication Laboratory, which is funded and managed by Virginia Tech's Institute for Critical Technology and Applied Science. Additional support is provided by the Virginia Tech National Center for Earth and Environmental Nanotechnology Infrastructure (NanoEarth), a member of the National Nanotechnology Coordinated Infrastructure (NNCI), supported by NSF (ECCS 1542100 and ECCS 2025151).